# Absorbance Modulation Optical Lithography

by

Hsin-Yu Sidney Tsai

Submitted to the Department of Electrical Engineering and Computer Science
in partial fulfillment of the requirements for the degree of

Master of Science in Computer Science and Engineering

at the

MASSACHUSETTS INSTITUTE OF TECHNOLOGY

September 2007

Author . . . . . . . . . . . . . . . . . . . . . . . . . . . . . . . . . . . . . . . . . . . . . . . . . . . . . . . . . .
Department of Electrical Engineering and Computer Science
Aug 31, 2007

Certified by . . . . . . . . . . . . . . . . . . . . . . . . . . . . . . . . . . . . . . . . . . . . . . . . . . . . . .
Henry I. Smith
Professor
Thesis Supervisor

Accepted by . . . . . . . . . . . . . . . . . . . . . . . . . . . . . . . . . . . . . . . . . . . . . . . . . . . . .
Arthur C. Smith
Chairman, Department Committee on Graduate Students

# Absorbance Modulation Optical Lithography

by

Hsin-Yu Sidney Tsai

Submitted to the Department of Electrical Engineering and Computer Science
on Aug 31, 2007, in partial fulfillment of the
requirements for the degree of
Master of Science in Computer Science and Engineering

## Abstract

In this thesis, the concept of absorbance-modulation optical lithography (AMOL) is described, and the feasibility experimentally verified. AMOL is an implementation of nodal lithography, which is not bounded by the diffraction limit of incident lights. Experimental results showed promising capability of AMOL and matched well with simulation. Several key elements of the AMOL system are discussed: the material systems of AMOL, limitations on the material and optical systems presented, and the design and fabrication of spiral phase elements that generate ring-shaped beams required by AMOL.

Thesis Supervisor: Henry I. Smith
Title: Professor

# Acknowledgments

First of all, I would like to thank all my advisor, Prof. Henry I. Smith, for providing constant support, constructive encouragement, useful guidance, broad picture of the world of lithography, and the freedom of proposing and testing out our own ideas.

I would like to give special thanks to Dr. Rajesh Menon, who has been working the most closely with me, providing solid optical simulation standings for experiments on AMOL, useful insights and valuable advice on both my research and English writing. Special thanks to Dr. Samuel W. Thomas, who is a great chemist and helpful collaborator, for helping us out with the synthesis and characterization of the Azo photochromic AML material, enabling us to demonstrate the feasibility of AMOL. Thanks to Prof. Karl Berggren for his insightful opinions on the introduction of the thesis.

I would also like to thank Jim Daley for his assistance in the laboratory, Dr. Feng Zhang and Mark Mondol for their valuable insights on the e-beam lithography system, Dr. Tymon Barwicz for help on profilometer, ellipsometer, Aquasave usage, and Raith 150 patterning strategy, Dr. Euclid Moon and Libby Shaw for assistance on AFM usage, Ta-Ming Shih, who has been a great officemate for this past year, for various useful discussions and support on a wide range of topics from school and lab work to living and software issues, Amil Patel for useful suggestions regarding oral presentation skills and slide preparation, Thomas B. O'Reilly for suggestions on the Lloyd's mirror system, the usage of PS-4, and characterizing photoresists, Dr. Tim Savas for suggestions on PMMA adhesion and advice on the optical contrast Lloyd's mirror, Bryan Cord for knowledge on PMMA development, Trey for help in resist property measurements with the ellipsometer, Joel Yang for valuable discussions on general processing issues, Jan Kupec for the assistance on using LaTeX, Dr. Juan Ferrera for suggestions on glass substrate processing with e-beam and the brushfire process, David Chao for his advice on the brushfire process, Dr. Ito Toshiki and Dr. Ji-Hyun Jang for sharing experiences in photo-initiator usage in photoresist, and Tiffany Kuhn for administrative supports.

Thanks to those of my friends who are also studying in the US, constantly reminding me that I'm not alone. Thanks to Jonathan, HueiHan, and Josh who accompanied and helped me through my first year at MIT. Special thanks to Jonathan, again, for teaching me how to learn to live an American life. Thanks to Kuang-Ting for sharing inspiring philosophy, the passion of studying physics, and your extraordinary cooking skills. Thanks to ChangAn for introducing me to the infinite world of board games. Thanks to Elaine, Charlene, Mong, and Wei-Ming who encourage me to travel in the US. Thanks to all the visitors: Tsung-Yu, Pitz, Feng-Hao, Wei-Yin, and Kate, who brought surprises to my life and made me learn more about the city I'm living in.

Thanks to all my friends I met at MIT. Thanks to Liang, Angelina, Amy, and Fei for sharing stories and feelings of ourselves. Thanks to Shirley and Jiye for your passion and responsibility on GW6 and on making EECS a more friendly place for female graduate students.

Thanks to all my friends and teachers from NEHS. You've always been the best listeners when I have things to share and always trigger me to think about the meaning of life. Thanks to the faithful militias in Taiwan for the constant support and Andrew koo, who translated this for me.

Thanks to Brian, who made me grow and learn a lot more about myself.

Thanks to Cherie, Joyce, and Esme, for the resonance among us all that cannot be described in words.

Thanks to my family, who has always supported my interests, my feelings, and my decisions. Thanks for teaching me the value of honesty and optimism, and the importance of always living a balanced life and care about others.

Thanks to Scott, who recently joined me and brought peace and joy to my daily life.

Thanks to the hardworking Sidney who always takes initiatives and measures herself with high standards.

Without you all, this thesis would not be possible.

# Contents

# List of Figures

# Chapter 1

# Introduction

## 1.1 Nodal Microscopy and Lithography

### 1.1.1 Beyond the Diffraction Limit

Conventional optical lithography techniques generate optical patterns by projecting an image of a physical mask, by scanning one or more tightly focused spots[1], by scanning near-field probes[2], or by exposure through a contact mask[3]. The first two are far-field techniques, and hence, limited by diffraction. One way to increase the resolution of such techniques is by decreasing the wavelength of illumination or by immersing the system in a medium with higher index of refraction, both of which often involve exceptional engineering challenges. Although the last two techniques are capable of sub-diffraction-limited patterning, they suffer from difficulties regarding the generation of the sub-wavelength aperture (usually with a mask) and gaping, which are described in section 1.2.1.

Alternative ways to surpass the diffraction limit for systems utilizing a focused light beam for microscopy or lithography is to utilize optical nonlinearities, such as multi-photon absorption[4], photoresist recording, and perfect lenses with negative refractive indices [5]. Multi-photon absorption usually requires high local light intensity, and the scaling of the full width at half maximum (FWHM) is inverse of the number of photons participating in the process, which is difficult to scale up. The high nonlinearity in the sensitivity curves of photoresists enables patterning of an arbitrary small spot by clipping close to the maximum of a point-spread-function(PSF) of light beam provided that there is infinitely accurate dose control. However, despite the infeasibility of such accurate dose control, the maximum intensity of a PSF usually fluctuates, giving large line-edge-roughness(LER) when pattering close to the maximum of the PSF. Additionally, since the Rayleigh criterion gives the minimum separation, $d$, of two simultaneously focused spots as $d = 1.22\lambda/NA$, where $\lambda$ is the wavelength of the light of illumination, and $NA$ is the numerical aperture of the focusing element, the ability of patterning arbitrary small spots with the nonlinearity of photoresists is limited to single spot or sparse feature exposures and does not really increase the patterning density. In contrast, dose control is achievable if we can pattern at the node instead of the peak of an intensity distribution, and the patterning density of such technique is not necessarily bound by the Rayleigh criterion. For example, in an optical node generated with a phase step, as shown in Fig. 1-1 (b), the change of sign of amplitude at the edge of the $\pi$-phase shifter ensures an absolute zero intensity at the edge. Unlike the case in Fig. 1-1 (a), where diffraction of light from the edge

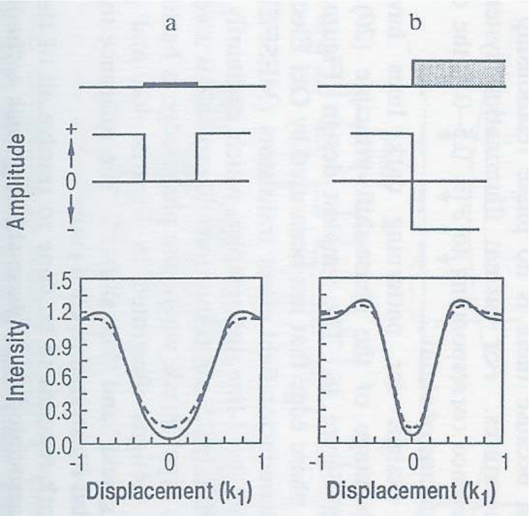

Figure 1-1: Techniques for generating an optical node. The mask structures are shown at the top, with the resulting amplitude profiles in the middle. At the bottom are the in-focus (solid lines) and out-of-focus (dashed lines) intensity profiles. (a) Conventional transmission mask. (b) Phase edge.[6]

begins to contribute to the nonzero intensity under the mask as the width of the mask decreases and the intensity of the incident light increases, the node in Fig. 1-1 (b) remains zero regardless of the incident light intensity. Therefore, providing exactly $\pi$-phase shift and unlimited incident light intensity, the light intensity at the node is absolutely zero, and the clipped feature size can be made arbitrary small with a fixed clipping dose without affecting the rest of the substrate. In reality, the capability of this technique is limited by the achievable light intensity, quality of the node, and the ability to pattern at a node. We will discuss several methods to pattern at the node in the rest of this chapter. The first method utilizes matastable-state atoms and a photo-quenching process to enable pattering at optical nodes. The other two methods illuminate a focused spot and an optical node at the same position, utilize nonlinearity in the optically active materials, and finally collect light or create patterns with ways developed for conventional optical microscopy and optical lithography. A similar idea of linearly subtracting the signal of a optical node from a conventional Gaussian PSF increased the resolution of a scanning optical microscope by a factor of two[7]. Note that although the size of each single node is not limited, the Rayleigh criterion still applies to the distance of two adjacent nodes simultaneously in focus.

In summary, the core idea of nodal microscopy and lithography is stated as follow: If there is a way one can detect signals or expose only at the nodes, instead of at the peaks of the light pattern, and collect signals or pattern from different positions incoherently (one after another), neither the feature sizes of each exposure nor the distance between patterns will be bound by the Rayleigh criterion.

### 1.1.2 Neutral-Atom-Beam Lithography

The idea of nodal lithography was first proposed in 1996[8] and demonstrated with neutral-metastable-atom lithography in 1998[9]. The metastable argon atoms used in the system have an energy spectrum as shown in Figure 1-2. An IR photon can bring the metastable argon atom to its excited energy state, which then radiatively decay to its ground state. Metastable argon atoms are capable of damaging the self-assembled monolayers[10] or prompting the deposition of carbonaceous film from vapor-phase

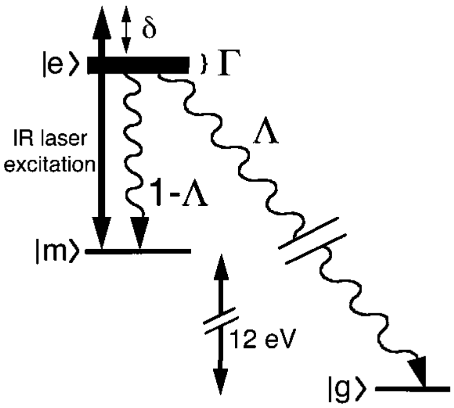

Figure 1-2: Simplified diagram of the argon level structure used for the neutral-atom nodal lithography system. An IR laser photon can excite the atom from the metastable state $| m >$ to an excited energy state $| e >$ that can radiatively decay to the atomic ground state $| g >$, dissipating the internal energy of the metastable state (12 eV) as a UV photon. Metastable argon atoms are able to induce carbonaceous film deposition on the surface of the substrate, while the ground-state argon atoms are not.[9]

hydrocarbon precursor upon collision with the surface[9], while ground-state argon atoms are not. The experimental set up is shown in Figure 1-3. A one-dimensional standing wave was created with an IR laser with a cylindrical symmetric Gaussian intensity profile to provide optical quenching of the metastable argon atoms as well as to optically confine the atoms towards the node of the beam. As a result, only atoms that pass through the nodes of the IR beam remain in their metastable states and interact to form carbonaceous structures on the substrate. Atoms that pass through the high IR light intensity regions are photo quenched to their ground states and do not interact with the substrate. The IR standing wave, therefore, acts as a virtually absorbing mask, letting only those metastable atoms very close to the nodes pass through without being quenched. This aperture can be made much smaller than the wavelength of the IR light, so what limits the feature size of the lines, in this case, is the Heisenberg uncertainty limit of the atoms. As shown in Fig. 1-4, a final pattern with 65nm FWHM, which is about $\lambda/15$, was achieved. Note that although the isolated feature size patterned with this technique is not limited by the Rayleigh criterion, the spacing between adjacent features, i.e. the period of the IR grating,

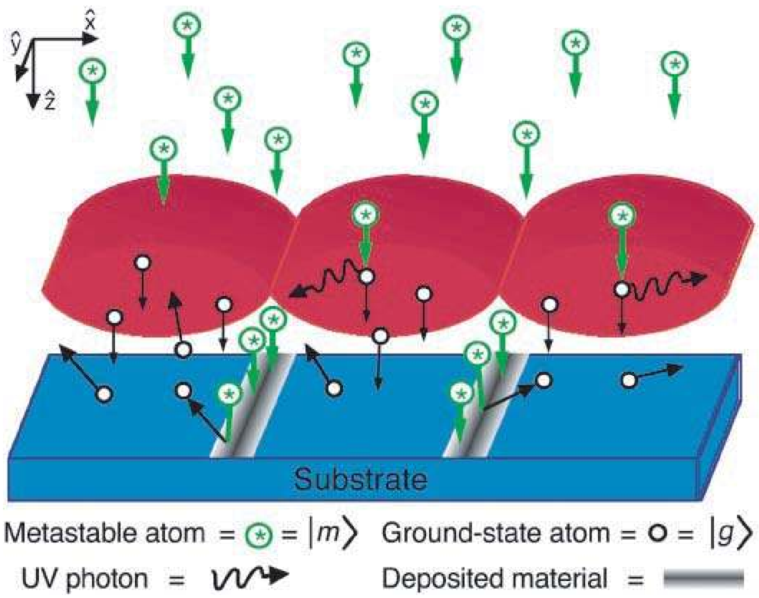

Figure 1-3: Schematic diagram of the experimental setup of neutral-atom nodal lithography. The 1D standing wave in IR spatially confines the argon atoms and optically quenches the metastable atoms everywhere except in narrow regions around the nodes of the standing wave. The transmitted metastable atoms interact with the surface and a background vapor precursor (not shown) to deposit a carbonaceous material. The achievable feature size with this technique is limited only by the matter-wave diffraction of atoms, which is negligible.[9]

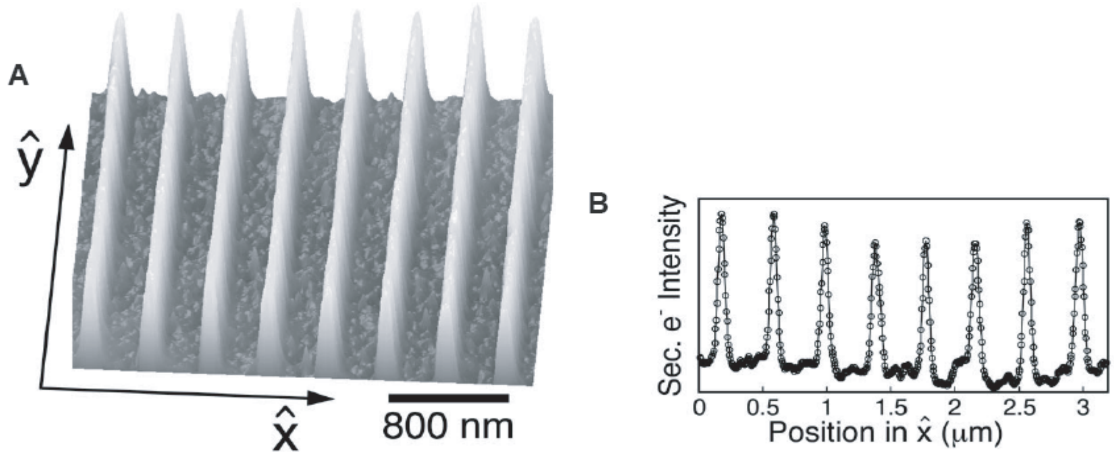

Figure 1-4: (A) AFM image of the pattern etched into a Si(110) substrate. The features etched into the silicon was 12 nm in height, while the original carbonaceous resist was only 0.6nm thick. (B) Average line profiles of SEM images were used to determine the width of the features. Analysis of the secondary electron intensity versus position indicates that the FWHM of the lines is 65 ± 0.5 nm.[9]

is. However, since the intermediate areas remain completely unexposed, one can fill in those areas to create dense grating patterns by translating the IR grating or the substrate by a fraction of the grating pitch and expose the substrate again.

### Limitation and Constraints

Although neutral-atom lithography demonstrated high-resolution lithographic capability, a number of obstacles must be overcome before this technique can become widely applicable for general lithographic purposes. First of all, the exposure times are typically hours due to faint atomic sources. The choice of atomic sources with proper photo-initiated metastable state transitions and the type of resists that would selectively react to the metastable state atoms is also limited. Second, the resists, or etch mask created by this technique, e.g. the carbonaceous films shown in the case above, are typically only 1nm. Therefore, the fabrication of any useful structures with higher aspect ratios requires an additional transferring step into the underlying substrate. Finally, the exposures must be performed in vacuum.

In summary, nodal lithography was successfully implemented with the neutral-atom lithography system by creating a sub-wavelength aperture for the patterning atoms close to the node of a far-field standing-wave light pattern. Neutral-atom lithography is advantageous for its potential capability of atomic resolution, no charging effects, and little damage to the substrate material because of the low atomic kinetic energies. However, it suffers from difficulties in the selection of atomic sources and recording resists, low throughput, and the fact that the lithography must be performed in vacuum.

## 1.1.3 Fluorescence Microscopy

Stefan W. Hell from the Max Plank Institute for Biophysical Chemistry, Department of NanoBiophotonics, Goettingen, Germany proposed the use of an optical node to break the diffraction limit in fluorescence microscopy. He called this as stimulated-emission-depletion (STED) fluorescence microscopy in 1994[11]. This concept of utilizing a reversible photo-induced transition between two states was later expanded to a three state system, as shown in Fig. 1-5 (a), to enable lithography[12]. State

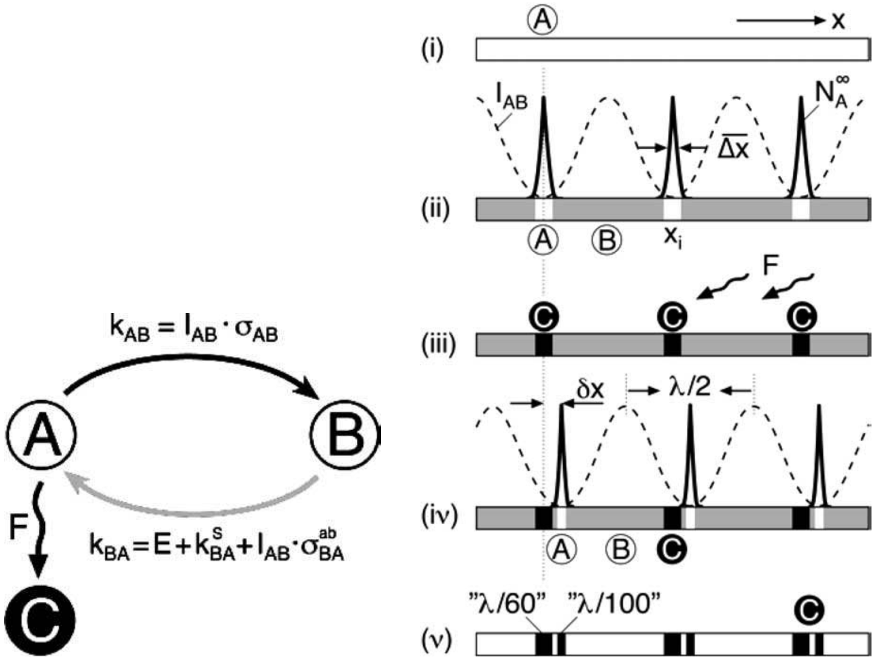

**(a)** **(b)**

Figure 1-5: (a) Diagram of state transition for nodal microscopy. A: the "active" state; B: the deactivated state. A→B is a saturable optical transition. B→A has no restrictions on the type of mechanism. Transition (F) to the irreversible state C enables writing of permanent structures. (b) Schematic of the lithography process with the states and transitions shown in (a). (i) The material is initially completely in state A. (ii) Expose the light that induces the saturable transition A→B to define sub-diffraction regions around the nodes at $x_i$. (iii) Impose the reaction A→C to create permanent structures on the sample. (iv) Shift the nodes by $\delta x$ and repeat the process in (ii) to place a similar structure at arbitrary proximity. (v) The lithographic linewidths can be adapted through the degree of saturation.[12]

A in Fig. 1-5 (a) represents the fluorescent excited state, or in general, the "active" state that allows emitting of light or patterning of the resist. State B represents the state that can be deactivated from state A with an efficient photo-induced process and can be brought back to state A with a separate process. State C represents an irreversible state that enables writing of permanent structures. For example, in neutral-atom nodal lithography, the metastable argon atoms would be state A, the ground-state atoms would be state B, and the carbonaceous film deposition induced by the collision of metastable atoms on the substrate would be state C.

The key step to this technique is the saturable A to B photo-induced transition, which deactivates state A, and ensures that parts illuminated with this light remain unexposed or cannot fluoresce, and leaves only those very close to the optical nodes in state A. Again, because the FWHM of the node is not bounded, the area that remains "active" is highly localized and does not suffer from the diffraction limit of the illuminating light(s). The signal collected from the remaining active states, therefore, represents only the information of that highly localized area, regardless of the diffraction limit imposed on the light that is actually collected. A schematic of applying this 3-state system to nodal lithography to achieve arbitrary dense patterns is shown in Fig. 1-5 (b). What's shown here is the same as the idea of re-exposing a spatially stepped substrate to pattern between nodes in neutral-atom lithography.

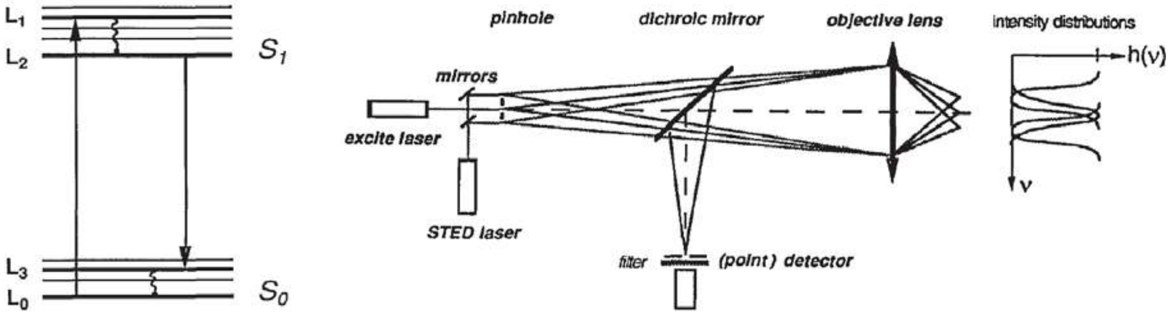

**(a)** **(b)**

Figure 1-6: (a) Energy levels of a typical fluorophore. (b) Schematic of the experimental setup for STED fluorescence microscopy. An excitation beam and the STED beams with a central node are focused for excitation and stimulated emission of the object. The beam intensity distribution is shown on the right. The spontaneously emitted light from the object is recorded in a (point) detector. Imaging was done by scanning the beams with respect to the object.[11]

Figure 1-6 (a) shows the energy levels of a typical fluorophore utilized in fluorescence microscopy. $S_0$ and $S_1$ are the ground and the first excited state, $L_0$ is the low vibrational level of $S_0$, and $L_1$ is the directly excited level of $S_1$, $L_2$ is the relaxed vibrational level of $S_1$, and $L_3$ is a higher level of $S_0$. Figure 1-6 (b) shows a schematic of the stimulated-emission-depletion (STED) fluorescence scanning microscope that was first proposed. The excitation light is focused and generates the $L_0$ to $L_1$ transition. The role of the STED beam is to induce the $L_2$ to $L_3$ transition by stimulated emission and to deplete the excited state before fluorescence takes place. The average fluorescence lifetime is of the order of 2 ns, the average vibrational relaxation time for $L_1$ to $L_2$ and $L_3$ to $L_0$ is typically 1-5 ps, and the quenching rate is typically $10^8 s^{-1}$. The vibrational relaxations are 3 orders of magnitude faster than the spontaneous emission $L_2$ to $L_3$. As stated in ref.[11], because of the dynamic nature of this process it is advantageous to use pulsed lasers with pulses significantly shorter than the average lifetime of $L_2$, i.e., pulses in the pico-second range. Temporal separation of the excitation and stimulated emission can be achieved by introducing a delay between the excitation and STED pulses. The optimal value of the temporal delay is such that the stimulated-emission pulse arrives as soon as the excitation pulse has ended since in that case, $L_2$ is not being populated while stimulated emission is taking place, so the depletion process of $L_2$ would be very efficient.

The STED beam is shaped to form a sub-wavelength node where the fluorescence is preserved. Improvements on the spatial quality of the STED beam[13] and the system were made over time, but the underlying mechanism remains the same. Recent results with STED fluorescence microscopy showed about $\lambda/50$ FWHM of the reduced focal spot, as shown in Fig. 1-7, and demonstrated the capability to optically distinguish two particles with $\lambda/10$ spacing[14].

### Limitations and constraints

The most obvious constraint for fluorescence microscopy is that the sample under observation must fluoresce. In addition, since the resolving power of STED fluorescence microscopy increases with the square root of the saturation level[14], high intensity quenching light may be required. Moreover, since the timing of the pulses are also critical to the depletion level, and, therefore, the system resolution, accurate control of the laser pulse widths and the delay between them is required. Finally, although STED works well for fluorescence microscopy, it has not yet been found possible to conduct lithography with this fluorescence system.

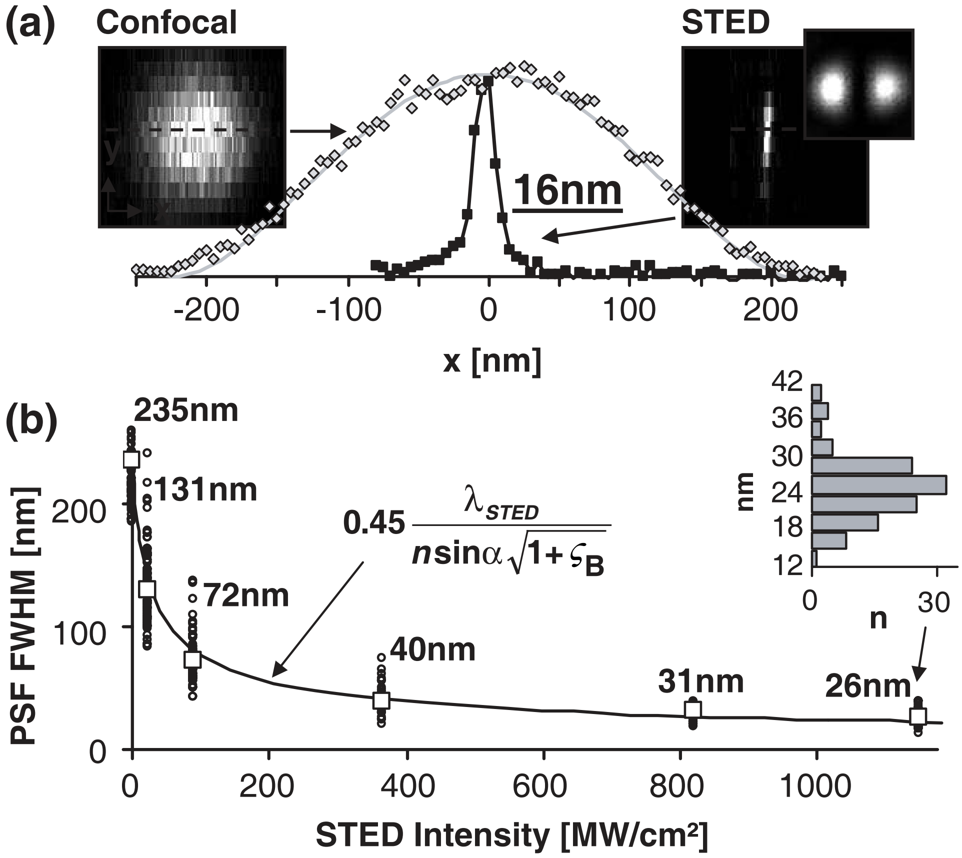

Figure 1-7: Reducing the fluorescence focal spot size to far below the diffraction limit: (a) spot of a confocal microscope (left) compared with that in a STED microscope (right) utilizing a y-oriented intensity valley for STED (upper right insert, not to scale) squeezing the spot in the x direction to 16 nm width. (b) The average focal spot size (squares) decreases with the STED intensity following a square-root law. Insert (right) discloses the histogram of the measured spot sizes rendering the 26 nm average FWHM.[14]

### 1.1.4 Absorbance Modulation Optical Lithography (AMOL)

A method applying a photochromic absorbance-modulation layer (AML) with one highly absorbing and one less absorbing state on top of the ordinary photoresist layer has been proposed[15]. Simulation showed that much higher resolution than that of the immersion technique could be achieved utilizing the two state absorbance and dichromatic transitions of the AML to modulate the transmitted point spread function[15]. A resolution of 30nm was predicted for patterns generated with a focused patterning beam and a ring-shaped modulation beam simultaneously illuminating the sample. This technique is called absorbance-modulation optical lithography (AMOL,) as shown in Fig. 1-8.

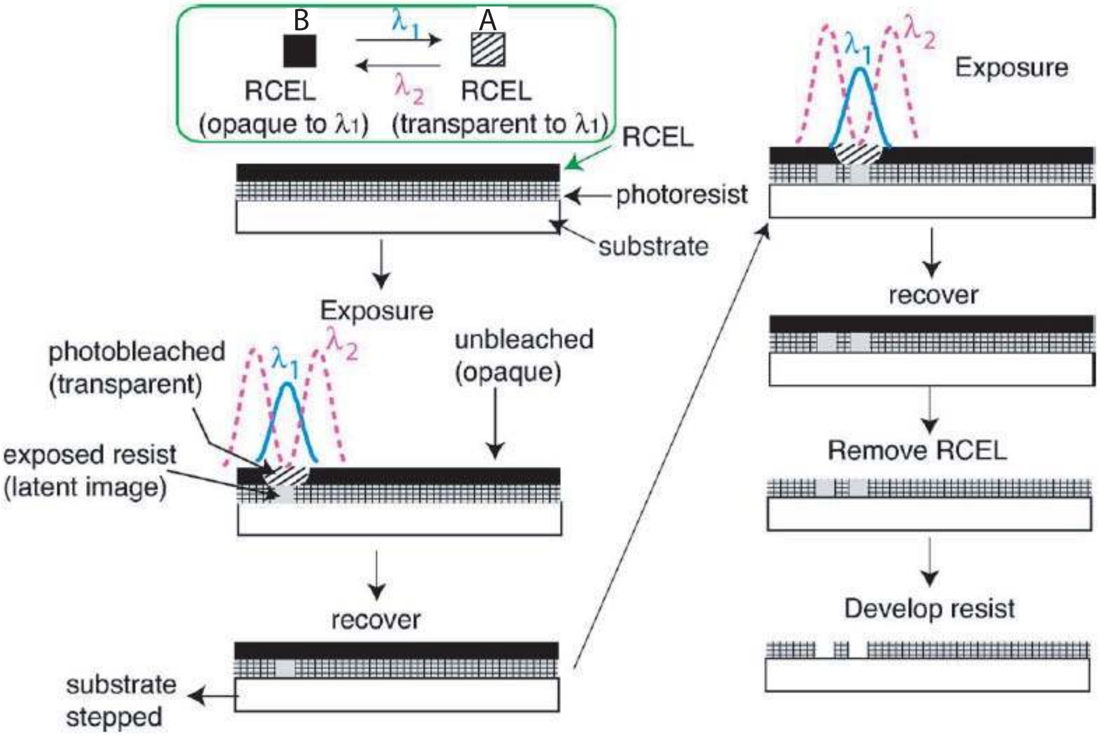

Figure 1-8: Schematic of AMOL. Note that the definition of configurations (A and B) is from that used in chapter 2. The ring illumination at $\lambda_2$ creates a local subwavelength aperture for $\lambda_1$, through which the underlying photoresist is exposed. After exposure, the AML recovers by exposure to $\lambda_2$. The substrate is stepped, and the $\lambda_1$, $\lambda_2$ exposure is repeated, effectively scanning the subwavelength aperture.[15]

Comparing the concept of AMOL to the diagram proposed by S.W. Hell in Fig. 1-

5 (a), the less absorbing state of AML would be the "active" state A, permitting the patterning light to penetrate through the AML; the highly absorbing state would be state B, preventing the light from passing. Illumination of light with wavelength $\lambda_1$ brings the AML from state B to state A, and the illumination of light with wavelength $\lambda_2$ brings the AML from state A to state B. However, instead of having the AML initially in state A, the default state for AML is the inactive state B. Moreover, the patterning process of the underlying photoresist induced by the light at $\lambda_1$ passing through the AML would not be classified as transition to state C in the scheme S.W. Hell proposed. There is a small, but substantial difference in how permanent structures are created between AMOL and the scheme presented in Fig 1-8. In the model shown in Fig. 1-5 (a), state C is arrived at from state A via an irreversible process. In contrast, the permanent structures in AMOL are created with light and an additional recording-material system, independent of the state switching in the AML. The state switching material, the AML, is only used to create a contact sub-wavelength aperture on top of the sample, either to conduct patterning in the case of lithography or to emit lights to be observed in the case of microscopy. The fact that the AML behaves independently of the recording stack facilitates the search on AML materials since the behaviors of the AML materials and recording materials can be optimized separately. Both photochromic materials and photoresist have been widely studied in the literature.

AMOL differs from neutral-atom nodal lithography and STED fluorescence microscopy in another important sense that the exposure condition is reached under photostationary dynamic competition between the A→B and B→A trasitions. Unlike in neutral-atom nodal lithography, where each argon atom is only pumped to its metastable state once over the process, and in STED fluorescence microscopy, where the fluorescence molecules are only excited once for signal collection at each position, both lights exposing the AML can be continuous lights, and there is no timing requirement.

However, since the aperture generated in the AML is sub-wavelength, the near-field lights that pass through can not propagate very far from the aperture, a thin (less than 30nm) resist, and, therefore, a process to transfer resist patterns to achieve high-aspect-ratio structures, the same as that mentioned in neutral-atom nodal lithography, are required.

The AMOL system will be described and discussed in detail in chapter 2.

## 1.2 The Zone Plate Array Lithography (ZPAL) System

### 1.2.1 Advantages of Optical Maskless Lithography

Although the main-stream patterning technologies in the current semiconductor industry still utilize mask-based lithography processes, the development of maskless lithography has provided promising possibilities for future technologies in terms of both resolution and throughput[1]. Patterning with a contact mask can achieve high resolution[3], but suffers from the requirement that an accurate mask is required in intimate contact with the substrate. Any defects in the mask or the substrate surface have significant deleterious effects on the generated patterns.

The zone-plate-array-lithography (ZPAL) systems have been developed in our lab with a 400 nm source and a resolution of 150 nm[16, 17]. Attempts to increase the resolution of ZPAL systems by applying immersion lithography have been made[18].

### 1.2.2 System overview

Figure 1-9 shows the schematic of the zone-plate-array lithography (ZPAL) system. Collimated beams modulated with a spatial-light modulator are sent to an array of binary-phase zone plates, generating an array of focused spots at the focal plane of the zone plates. With this simple optical design, massively parallel beams ($10^3$-$10^6$) are achievable. By scanning the substrate on the stage, arbitrary patterns can be written in a dot-matrix fashion. The resolution of ZPAL is limited by the Rayleigh criterion, but can be extended by using shorter patterning wavelength or by the use of absorbance-modulation.

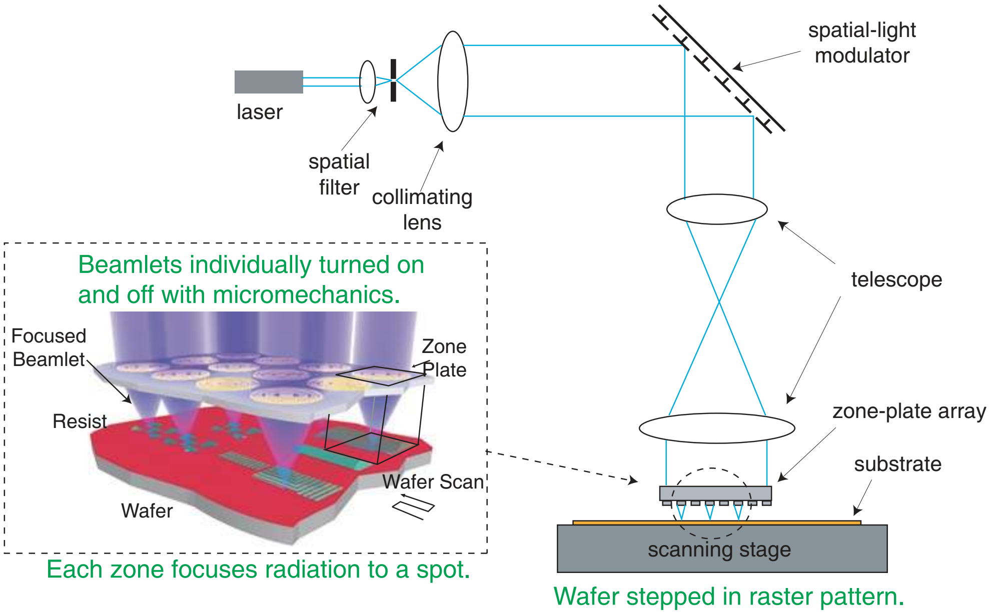

Figure 1-9: Schematic of the zone-plate-array lithography (ZPAL) system. An array of Fresnel zone plates focuses the incident collimated beamlets. By scanning the substrate on a stage, arbitrary patterns are written in a dot-matrix fashion.

### 1.2.3 Integration of AMOL on ZPAL

AMOL can be integrated with ZPAL to obtain sub-wavelength resolution and high throughput at the same time. Figure 1-10 shows a schematic of such integration. In this schematic, the zone plate array is replaced with a dichromatic plate array. The dichromatic plate array gives the exposure condition of AMOL, which corresponds to a focused spot for the $\lambda_1$ beam and a donut-shaped spot with a central node for the $\lambda_2$ beam, as shown in Figure 1-11.

One way to fabricate the dichromatic plate is to combine the zone plate array and spiral phase elements. The inner zones of the zone-plate array are replaced by spiral phase elements. Wavelength-filtering layers are coated on the back of the dichromatic-plate array so that only $\lambda_2$ light passes through the spiral-phase plate, and only $\lambda_1$ light passes through the rest of the plate. The spiral phase element at the center creates the null at $\lambda_2$ required for AMOL, and the outer zones of the zone plate focus the beam at $\lambda_1$, but with a lower efficiency. Because the diffractive optical patterns of the dichromatic plate can be fabricated with a single scanning-electron-beam lithog-

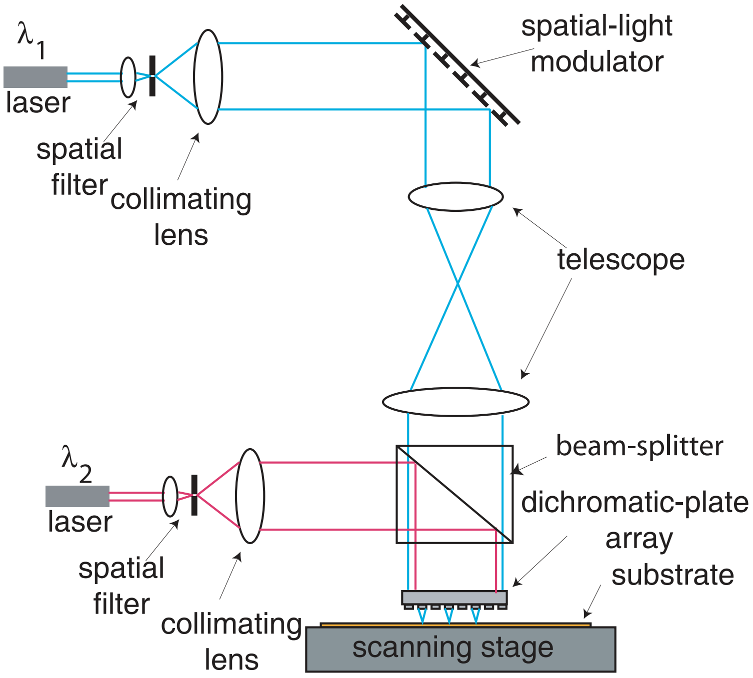

Figure 1-10: The scheme of AMOL integrated with a ZPAL system. Collimated laser beams with wavelength $\lambda_1$ and $\lambda_2$ are sent into the dichromatic-plate array, which focuses the $\lambda_1$ beam and creates the donut-shaped profile for the $\lambda_2$ beam.

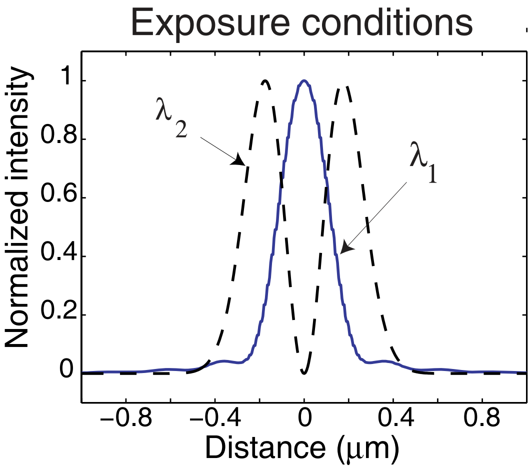

Figure 1-11: Exposure condition for AMOL. The beam shape is axially symmetric. With proper design, the donut-shaped $\lambda_2$ beam suppresses the bleaching of the tails of the main lobe of $\lambda_1$ beam though the AML, resulting in a sharper patterning beam and higher resolution.

raphy step, the focused spot and donut-shaped beam the dichromatic plate generates would be automatically aligned. The only alignment step required in this process is coating the wavelength-filtering layers. Other designs, including designing a modified zone plate that simultaneously focuses the $\lambda_1$ beam while creating a central node of the $\lambda_2$ beam, are also under investigation.

## 1.3 Organization of Thesis

In this thesis, the concept of absorbance-modulation optical lithography (AMOL) is described, and the feasibility experimentally verified. In chapter 2, a model to simulate AMOL is proposed, and several key elements of the AMOL system discussed. In chapter 3, several material systems of AMOL are described. In chapter 4, experimental results that demonstrate the capability of AMOL and limitations on the material and optical systems are presented. In chapter 5, the design and fabrication results of spiral phase elements that generate the ring-shaped beams with central nodes are shown.

# Chapter 2

# Absorbance Modulation Optical Lithography (AMOL)

In this chapter we describe the implementation of absorbance-modulation optical lithography (AMOL) to overcome the diffraction limit. We show by simulation that AMOL enables the focal-spot approach to achieve a lithographic resolution that is 1/13th of the wavelength. We also verify that absorbance modulation represents an optical nonlinearity that depends on the ratio of two independent intensities and not on the absolute intensity of either one alone. By choosing the appropriate ratio of power densities at the two wavelengths, the width of the transmitted lines can be significantly smaller than the diffraction limit. This technique, therefore, opens up the possibility of generating optical near fields with far-field optics.

## 2.1 The Absorption Modulated Optical Lithography (AMOL) System

The concept of the AMOL system relies on the reversible photochromic property of the Absorbance Modulation Layer (AML), as shown in Figure 2-1. The exposure of a beam of light with wavelengthl $\lambda_1$ converts the originally highly absorbing AML configuration A to a less absorbing configuration B. The light at $\lambda_1$ then penetrates the AML and exposes the underlying photoresist. If we turn off the exposing light, the AML can either thermally return to its original configuration or be brought back to the high absorbance configuration B by exposing the AML to another beam with wavelength $\lambda_2$. Note that it is crucial that the wavelength $\lambda_2$ does not expose the photoresist while converting configuration B back to configuration A. This reversible photochromic property has been widely studied in the reversible contrast enhancement layer (RCEL) and referred to as bleachable absorption[19] and reversible bleaching[20].

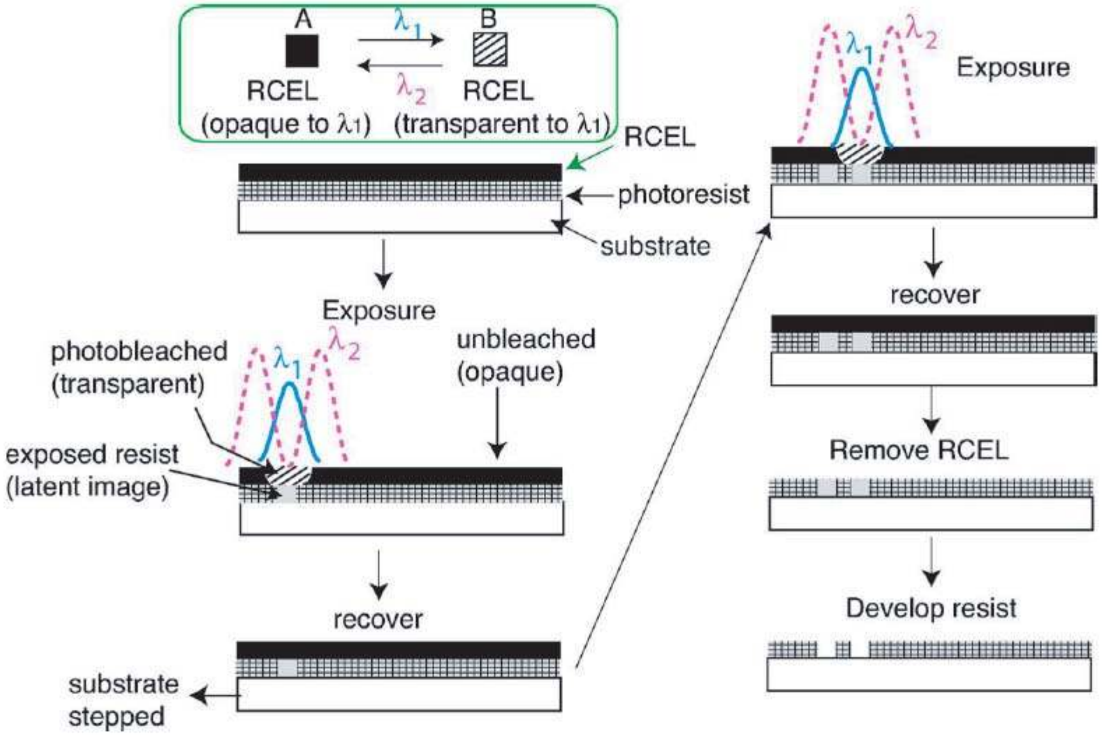

Figure 2-1: Schematic of AMOL. The ring illumination at $\lambda_2$ creates a local subwavelength aperture for $\lambda_1$, through which the underlying photoresist is exposed. After exposure, the AML recovers by exposure to $\lambda_2$ or thermally. The substrate is stepped, and the $\lambda_1$, $\lambda_2$ exposure is repeated, effectively scanning the subwavelength aperture.[15]

By simultaneously illuminating the layers with a focal spot at the bleaching wavelength $\lambda_1$ and a ring-shaped illumination at the reversing wavelength $\lambda_2$, the dynamic competition in the AML results in a transmission aperture at the bottom of the AML that is much narrower than the case without the AML effect. In other words, because of the designed ring-shaped light at $\lambda_2$, the bleaching process through the AML at the sides of the main lobe and side lobes of the $\lambda_1$ beam can be selectively suppressed, resulting in a much sharper transmitted point-spread function (PSF) at the photoresist layer. The exposure condition and compression of the PSF are shown in Figure 2-2. Once the exposure of a given spot is completed, a second exposure can be carried out adjacent to the first at a separation that is significantly smaller than the width of the original $\lambda_1$ input PSF, as shown in Fig. 2-1.

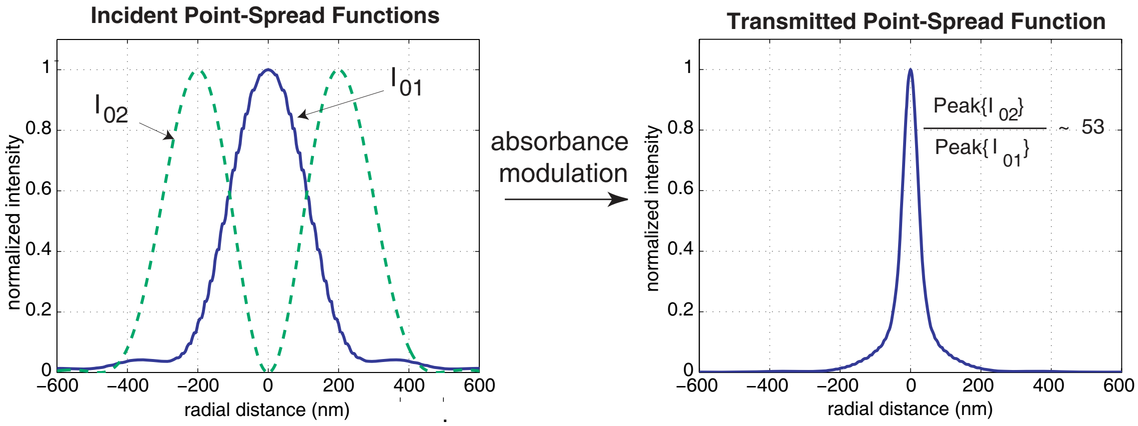

Figure 2-2: Exposure condition and PSF compression for AMOL. The beam shape is axially symmetric to the d=0 axis. With proper design, the main peaks of $\lambda_2$ beam overlap the side lobes of $\lambda_1$ beam and therefore suppresses the bleaching of the side lobes of $\lambda_1$ beam though the AML, resulting in a sharper patterning beam and higher resolution. $I_{01}$ is the intensity of the $\lambda_1$ beam, and $I_{02}$ is the intensity of the $\lambda_2$ beam. Simulation results done by Rajesh Menon

The nonlinearity that enables the compression of the transmitted $\lambda_1$ PSF is introduced by the reversible photochromic property of the AML, and the structured illumination at the two wavelengths. It is not dependent on large light intensities, but utilizes the concept that a null in optical intensity, such as realized via phase steps, is not bound by the Rayleigh criterion. In fact, the phase-step concept is employed in modern optical lithography[21]. In the next section, we show that the resulting nonlinearity is dependent on the ratio of the intensities at the two wavelengths, not on either one alone, and hence, is not limited by the diffraction limit imposed by either one.

## 2.2 Theory, simulation results, and the resolution limit of AMOL

### 2.2.1 Modeling AMOL

AMOL was modeled as a time-dependent absorbance variation layer with a thickness much less than the wavelength $\lambda_1$. In this model, we assume no back reflection from the substrate under the photoresist. The relation between the incident light intensity and the exposure dose on the top surface of the photoresist can be expressed as

$$D(r,\tau) = I_{01}(r)\int_0^{\tau} 10^{-\alpha_1(r,t)}dt \tag{2.1}$$

where $I_{01}(r)$ is the light intensity at $\lambda_1$ incident on the top surface of the AML, $r$ is the position on the surface, $\tau$ is the exposure time, and $\alpha_1$ is the absorbance at $\lambda_1$ of the photochromic layer.

From the Beer-Lambert equation,

$$\alpha_1(r,t) = \alpha_{1A} + \alpha_{1B} = \{\epsilon_{1A}[A(r,t)] + \epsilon_{1B}[B(r,t)]\}l \tag{2.2}$$

where $[A(r,t)]$ and $[B(r,t)]$ are the concentrations of configurations A and B, respectively, in the AML; $\epsilon_{1A}$ and $\epsilon_{1B}$ are the molar absorption coefficients of A and B configurations at $\lambda_1$; and $l$ is the thickness of the AML. The fraction of the incident $\lambda_1$ radiation that is absorbed is given by[20]

$$f_1(r,t) = \frac{I_{01}(r)}{l}[1 - 10^{-\alpha_1(r,t)}] \tag{2.3}$$

Assuming that the fraction that was absorbed by the A configuration all contributes to the A to B transformation, this fraction is given by

$$f_{1A}(r,t) = \frac{I_{01}(r)}{l}(1 - 10^{-\alpha_{1A}(r,t)})\frac{\alpha_{1A}(r,t)}{\alpha_1(r,t)} = \frac{I_{01}(r)}{l}F_1(r,t)\alpha_{1A}(r,t) \tag{2.4}$$

where $F_1$ is called the photokinetic factor at $\lambda_1$, and $\alpha_{1A}$ is the absorbance due to configuration A only, as indicated in Eq. 2.2.

Our absorbance model must take into account that thermal conversion can occur from B to A, the stable lower-free-energy configuration, but not from A to B. Also, while $\lambda_1$ predominantly converts A to B, it also converts B to A, but at a lower efficiency. Similarly, while $\lambda_2$ predominantly converts B to A it also converts A to B, but at a much lower efficiency.

The change in the concentration of A as a function of time during exposure can be written as

$$\begin{aligned} -\frac{d[A(r,t)]}{dt} = \quad & \phi_{1AB}\tfrac{I_{01}(r)}{l}F_1(r,t)\alpha_{1A}(r,t) + \phi_{2AB}\tfrac{I_{02}(r)}{l}F_2(r,t)\alpha_{2A}(r,t) \quad -k_{BA}[B(r,t)] \\ & -\phi_{1AB}\tfrac{I_{01}(r)}{l}F_1(r,t)\alpha_{1B}(r,t) - \phi_{2AB}\tfrac{I_{02}(r)}{l}F_2(r,t)\alpha_{2B}(r,t) \end{aligned} \tag{2.5}$$

where $\phi$ is the quantum efficiency of the subscript designated transformation, the subscript 2 refers to illumination by $\lambda_2$, and $k_{BA}[B(r,t)]$ is the rate of thermal conversion from B to A. Finally, from conservation of mass,

$$[A]_0 = [A] + [B] \tag{2.6}$$

where we assumed that only species A is present initially, with a uniform concentration of $[A]_0$. Substituting Eqs. 2.6 and 2.2 into Eq. 2.5 yields

$$\begin{aligned} & -\frac{d[A(r,t)]}{dt} = \\ & [(\phi_{1AB}\epsilon_{1A} + \phi_{1BA}\epsilon_{1B})I_{01}(r)F_1(r,t) + (\phi_{2AB}\epsilon_{2A} + \phi_{2BA}\epsilon_{2B})I_{02}(r)F_2(r,t) + k_{BA}][A(r,t)] \\ & -[k_{BA} + \phi_{1BA}\epsilon_{1B}I_{01}(r)F_1(r,t) + \phi_{2BA}\epsilon_{2B}I_{02}(r)F_2(r,t)][A]_0 \end{aligned} \tag{2.7}$$

By numerically solving Eq. 2.7, we can evaluate the transient behavior of absorbance under illumination.

From the information of absorbance chance over time, we can numerically integrate Eq. 2.1 to obtain the light intensity at the top of the photoresist layer from the incident light intensity. Furthermore, if the exposure time $\tau$ is chosen such that the photostationary state is reached at all points, then we can approximate Eq. 2.1 as

$$D(r,\tau) \approx I_{01}(r)\int_0^{\tau} 10^{-\alpha_{1PS}(r)}dt = I_{01}(r)\tau(10^{-\alpha_{1PS}(r)}) \tag{2.8}$$

where $\alpha_{1PS}(r)$ is the absorbance in the photostationary state at $r$. Because the initial absorbance is high compared with $\alpha_{1PS}(r)$, the contribution to the transmitted PSF, $D(r,\tau)$, during the initial transient is intrinsically smaller. The approximation of Eq. 2.8 is valid even when $\tau$ is not much larger than the duration of the transient, because the absorbance enters into the exponent.

To gain more insight into this model, we can simplify the results by computing its photostationary state so that Eq. 2.7 goes to zero and assuming a negligible thermal rate constant $k_{BA}$. Equation 2.7 then becomes

$$[(\phi_{1AB}\epsilon_{1A} + \phi_{1BA}\epsilon_{1B})F_1(r) + (\phi_{2AB}\epsilon_{2A} + \phi_{2BA}\epsilon_{2B})\frac{I_{02}}{I_{01}}F_2][A(r)] = \\ [\phi_{1BA}\epsilon_{1B}F_1 + \phi_{2BA}\epsilon_{2B})\frac{I_{02}}{I_{01}}F_2][A]_0 \tag{2.9}$$

and the final absorbance $\alpha_{1PS}(r)$ is

$$\alpha_1(r) = [(\epsilon_{1A} - \epsilon_{1B})[A(r)] + \epsilon_{1B}[A]_0]l \tag{2.10}$$

Note that in Eq. 2.9, $[A(r)]$ and, therefore, $\alpha_{1PS}(r)$ is dependent only on the ratio of the intensities $I_{02}(r)/I_{01}(r)$, but not on the absolute intensities themselves. If we look at the extreme cases of $I_{02}(r)/I_{01}(r) \rightarrow \infty$ and $I_{02}(r)/I_{01}(r) \rightarrow 0$, we get

$$[A(r)] = [A]_0\frac{\phi_{2BA}\epsilon_{2B}}{\phi_{2AB}\epsilon_{2A} + \phi_{2BA}\epsilon_{2B}} \tag{2.11}$$

for $I_{02}(r)/I_{01}(r) \to \infty$, and

$$[A(r)] = [A]_0 \frac{\phi_{1BA}\epsilon_{1B}}{\phi_{1AB}\epsilon_{1A} + \phi_{1BA}\epsilon_{1B}} \tag{2.12}$$

for $I_{02}(r)/I_{01}(r) \to 0$ In order to achieve maximum contrast in the photostationary absorbance, we would like our optical contrast, which is represented by the modulation of the $I_{02}(r)/I_{01}(r)$ term, to convert efficiently into the modulation of $[A(r)]$. Therefore, in Eq. 2.11, $[A(r)]$ should be as close to $[A]_0$ as possible, while in Eq. 2.12, $[A(r)]$ should be as close to 0 as possible. These constraints can be alternately described by the following conditions

$$\frac{\phi_{1AB}}{\phi_{1BA}}\frac{\epsilon_{1A}}{\epsilon_{1B}} \gg 1 \tag{2.13}$$

$$\frac{\phi_{2BA}}{\phi_{2AB}}\frac{\epsilon_{2B}}{\epsilon_{2A}} \gg 1 \tag{2.14}$$

which simply mean the absorption of $\lambda_1$ should be much higher for configuration A than B, and $\lambda_1$ illumination should trigger the A to B transformation much more efficiently than the reversed transformation (same applies for $\lambda_2$ illumination and the B to A transformation). These conditions agree well with the picture of the ideal behavior of the AML.

One last thing to note is that because the final image contrast at the top of the photoresist depends on the contrast of the photostationary absorbance and the final exposure dose, high contrast only in the modulation of $[A(r)]$ is not enough. Eq. 2.10 shows that the contrast in $[A(r)]$ translates into the final absorbance contrast through a factor of $(\epsilon_{1A} - \epsilon_{1B})$). Therefore, high initial absorbance of the AML material, $\epsilon_{1A}$, is also important to the final image contrast.

### 2.2.2 Simulation results

From the above models we can simulate the AMOL point spread function (PSF) using parameters for the AML. Details on the calculations and parameters used can be found in ref. [15]. Figure 2-3 shows the calculation results of a highly compressed PSF (the

AMOL PSF), which determines the major lithographic figures of merit, at the top of the photoresist layer. If the assumptions for Eq. 2.9 are satisfied, the compression of the PSF is only dependent on the absorbance distribution in the photostationary state, independent of the absolute intensities at $\lambda_1$ and $\lambda_2$. In fact, higher incident intensities only shorten the time to reach the photostationary state and the exposure time. It should be noted that since a significant amount of incident light is absorbed in the AML, the efficiency of light transmission is quite low. By going to shorter wavelengths, one can clearly achieve narrower focused spots and rings, and hence a narrower transmitted (or AMOL) PSF as well.

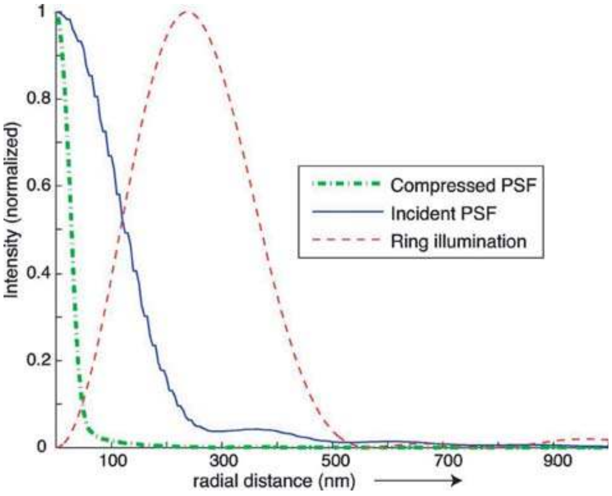

Figure 2-3: PSF compression via AMOL. During exposure by a focused spot at $\lambda_1$, a ring-shaped spot at $\lambda_2$ also illuminates the same area as shown. Illumination at $\lambda_2$ suppresses the conversion from A to B except at the center of the spot, where its intensity is 0.[15]

A grating of 50% duty cycle was used as a test pattern to evaluate the contrast in the final aerial image and compare it with the image contrast obtained with the uncompressed PSF. Figure 2-4 shows the aerial-image contrast as a function of the half-pitch of a grating. As expected, the contrast decreases with decreasing half-pitch. A plot for the uncompressed PSF is also shown. We have experimentally demonstrated 135 nm half-pitch gratings using this uncompressed PSF[18], which corresponds to an aerial image contrast of 0.12. For the same image contrast, the half-pitch obtained with the compressed (AMOL) PSF would be 30 nm. Thus, the simulation indicates that AMOL should be capable of printing features that are smaller than $\lambda/13$ with spatial periods far below the Rayleigh resolution criterion. The improvement in image contrast via AMOL is achieved through the reduction of the width of the mainlobe of the PSF as well as the suppression of the major sidelobes. This latter suppression has the important result of reducing proximity effects.

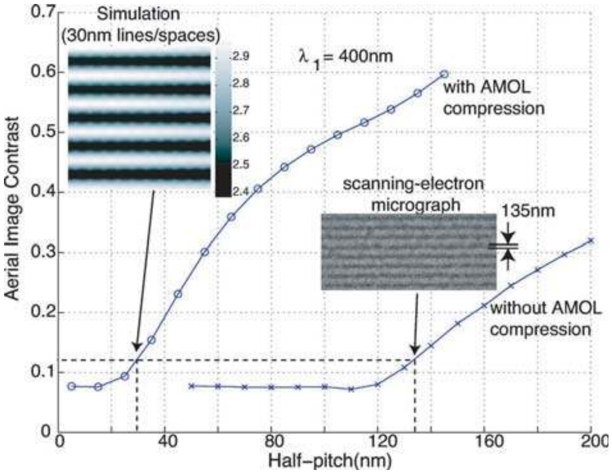

Figure 2-4: Aerial image contrast of grating patterns as a function of the grating half-pitch with and without AMOL compression. The scanning-electron micrograph of 135 nm lines and spaces was patterned using an uncompressed PSF at $\lambda_1$=400 nm and NA=0.85.[18, 15]

## 2.3 Key elements to the AMOL System

According to the design and simulations discussed in previous sections, this section summarizes the key elements that determine the feasibility and resolution capability of AMOL. In chapter 3, we describe in detail the material system for the AML and the recording stack mentioned in section 2.3.1 and 2.3.2. In chapter 4, we experimentally characterized the spatial structure of this localized light field with the material systems described in chapter 3, and compared it against the theoretical model. Finally, in chapter 5, we demonstrate the fabrication of diffractive optical devices to obtain the ring-shaped beam for $\lambda_2$, as discussed in section 2.3.3.

### 2.3.1 AML properties

The most obvious constraint on the AML is its reversible photochromic transitions. However, there are many subtle, but important parameters regarding this transition process that greatly affects the capability of AMOL, such as the absorbance contrast, transition speed, thermal stability, and the transition wavelengths. In fact, there is no perfectly transparent or opaque state for any material and the transition between the two states is not 100% efficiency. The idealized picture of AMOL is good for describing the concept, but in reality there is always a compromise between perfect material properties and perfect resolution.

#### The absorbance contrast

Since there are neither perfect transparent nor opaque states of a material, what we are concerned with here is the absorbance contrast. The absorbance contrast is defined as the absorbance for configuration A over the absorbance for configuration B at $\lambda_1$. For example, Fig. 3-2 shows the UV-Vis absorbance spectra of one of our AML materials. The absorbance contrast is about 4 in that case and is shown in chapter 4 to be sufficient to provide enough modulation in the AML to demonstrate AMOL.

Note that section 2.2.1 shows that not only the absorbance contrast, but the absolute absorbance for configuration A determines the final image contrast after passing through the AML. Although we can always increase the absolute absorbance by using thicker AML, because light also diffracts within the AML, the final image contrast decreases as the thickness of the AML increases and, therefore, limits the maximum thickness of the AML. One way to increase the absolute absorbance is to increase the density of the photochromic molecules by polymerizing small molecules and adding plasticizers.

#### The photo-transition speed

The ratio of the two photo-transition speeds from A to B and from B to A determines the physical power ratio one needs to apply to achieve the desired dynamic PSF formed in the AML. The absolute photo-transition speed from A to B determines the transient time before the AML reaches its photostationary state. Usually it is desirable to have a faster transition from B to A, preventing the AML from over bleaching and exposing the underlying photoresist during the transient state.

### Thermal stability

Thermal instability of the AML is not desirable, as discussed in section 2.2.1. We showed that if $k_{BA} = 0$, implying thermal stability of the AML, the modulation in the AML and therefore the final PSF passing through the AML only depends on the $I_{01}/I_{02}$ ratio, but not on either intensity. However, when thermal instability is included, thermal conversion speed from configuration B back to configuration A sets an absolute scale which the light intensity at $\lambda_1$ would have to overcome in order to bring the absorbance of the AML down enough to efficiently expose the underlying photoresist. Fig. 2-5 compares the scaling of full width half maximum (FWHM) with $\lambda_2$ to $\lambda_1$ power ratios for cases with and without thermal instability. It can be seen clearly that thermal instability imposes a limit on the scaling of the FWHM and also increases the required power ratio $P_2/P_1$ to achieve the same FWHM. Extremely high $P_2/P_1$ is also undesirable because heating effect becomes dramatic when the one of the laser powers becomes high or when the exposure time becomes long. Note that in Fig. 2-5, the calculations were done assuming perfect optical node at the center for $\lambda_2$. The effect of thermal instability can also be thought of as imposing a uniform background illumination at $\lambda_2$, resulting in an imperfect node.

### The transition wavelengths

Not all transition wavelengths will work. In order to construct the high quality focused beam and ring-shaped beam, a proper laser light source is required. In addition, the requirement that $\lambda_2$ does not expose the underlying photoresist implies that $\lambda_2$ needs to be larger than $\lambda_1$ and $\lambda_2$ cannot be too close to $\lambda_1$, depending on the photoresist property.

Other less important properties include the ease of film processing. Small molecules

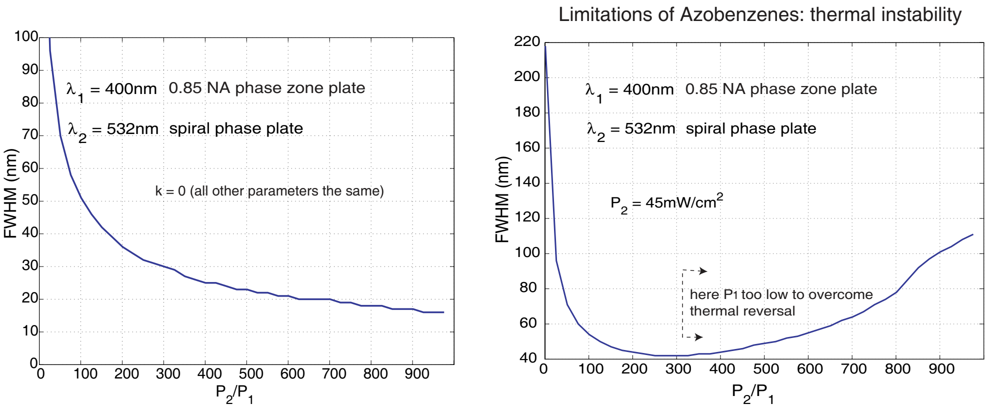

**(a)** **(b)**

Figure 2-5: The scaling of full width half maximum (FWHM) with power ratios $P_2/P_1$ (a) with and (b) without thermal instability. Thermal instability imposes a limit on the scaling of the FWHM and also increases the required power ratio $P_2/P_1$ to achieve the same FWHM. Simulations were done by Rajesh Menon.

segregate easily, so it's difficult to make uniform films out of them. In contrast, long chain polymers are usually easier to spin-coat in solution. In the experiments described in this thesis, small molecules are dissolved in a polymer matrix with the highest concentration possible before molecular segregation occurs, while polymers are spin-coated directly.

### 2.3.2 Recording stacks properties

The recording stack under the AML is a photoresist-based stack modified to accommodate the AML behavior. Because the AML needs to be removed after the exposure, but before photoresist development, we must be able to remove the AML without affecting the underlying photoresist. However, most solvents of the AML do affect the photoresist, so even spinning the AML on top would degrade the photoresist property. Therefore, a protection layer is required, and will be discussed in the following chapter.

The photoresist should be insensitive to $\lambda_2$, while having a reasonable (as high as possible, exposure time should be less than 2hrs) sensitivity to $\lambda_1$. In addition to having high resolving power, the photoresist should be able to work at a resist thickness as thin as possible because the light that transmits through the sub-wavelength aperture formed in the AML is the near field component, which does not propagate very far. The stack would, therefore, need to be transferable to a bottom stack to create higher-aspect-ratio structures.

### 2.3.3 The optical properties of the system

The node quality of $\lambda_2$ is critical to the aperture formation in the AML and the final image contrast. The null at the center of the ring-shaped illumination ensures that the conversion from the opaque A configuration to the transparent B configuration is maximized there, while everywhere else the conversion is reduced. The quality of the node has a great effect on the full width half maximum (FWHM) of the PSF reaching the photoresist layer. As shown in Fig. 2-6, a resolution limit is imposed on the scalability of the FWHM with only a 1% background. In the experimental setup that will be discussed in chapter 4, the background is typically 3%. In addition, the $\lambda_1/\lambda_2$ intensity ratio in that case was also limited due to limited laser power and lack of focusing ability of the system setup. These two optical properties greatly affect the resolution one can achieve, and should be taken into serious consideration when building the optics.

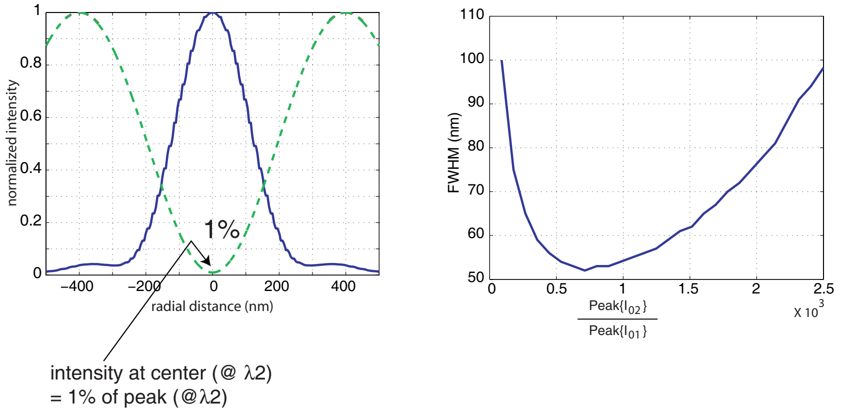

Figure 2-6: The effect of an imperfect node in the $\lambda_2$ beam. The figure on the left shows the optical intensity distributions of the two beams, and the figure on the right shows the FWHM scaling with power ratio under the presence of the 1% background. Simulations were done by Rajesh Menon.

# Chapter 3

# The Recording Stack

## 3.1 The Stack Design

### 3.1.1 The Stack and the Development Procedure

The substrate consisted of pieces of silicon wafer that were spin coated with 200 nm of antireflection coating, BarLi (Microchemicals, Germany), photoresist, 24 nm of poly vinyl alcohol (PVA), and 200 nm of absorbance modulation layer (AML) in that order. Only the AML is not pre-baked, but left to dry to drive away the remaining solvent because it was found that pre-baking causes intermixing between the AML and PVA layers.

After exposure, the AML was removed by dipping in trichloroethylene for 30 s. This was followed by a 30 s rinse in DI water to remove the PVA layer. The PVA acts as a barrier layer, protecting the underlying photoresist during the removal of the AML. It also prevents the intermixing of the AML and the photoresist. The substrate was then treated with a post-exposure bake on a hotplate if necessary. Finally, the substrate was developed with the proper developer for the photoresist. The developed patterns in photoresist were sputter coated with about 1 nm of a Pd/Au alloy before inspection in a scanning-electron microscope.

### 3.1.2 Chemical Compatibility of the Stack

As discussed in section 2.3.2, the role of the thin PVA layer, separating the AML from the photoresist, is critical for the AMOL system because it provides the barrier between the optics and the recording layer. However, PVA is not resistant to all solvents. PVA is a water soluble material that does not dissolve in many organic solvents, but strong solvents, such as acetone, still dissolves PVA immediately. This limits the type of solvents one can choose for dissolving the AML for spin-coating purposes and for removing the AML layer. For dissolving AML, we find that our current PVA process works well with chloroform and anisole, but we encountered more difficulties on removing the AML.

The removal of the AML is simply by dissolving the AML with the stripping solvent. Therefore, any solvent that can dissolve the dye well, and does not affect or penetrate through the PVA layer should work well as a stripper. However, we found that even trichloroethylene, which we used in the standard AML removal process for all the results shown in the next chapter, affects the underlying photoresist through the 24nm thin PVA layer. Results show that the development rate of the resist slowed down after the 30s trichloroethylene dip, confirming that the protection of PVA is not perfect. The increase in exposure dose is undesirable because long exposure time introduces more vibration, drifting, and local heating problems and decreases the overall throughput. Ways to improve this problem include using other solvents with lower boiling points, such as 1,2-dichloroethane, or using a thicker PVA layer. Unfortunately, searching for a proper solvent and testing the level of effect to the underlying resist for each AML is very time consuming and impractical. Moreover, since the near-field light passing through the sub-wavelength aperture formed in the AML do not propagate very far, the PVA layer is required to be as thin as possible.

An alternative method of removing the AML and PVA layer is by putting the sample into water and applying ultrasonic agitation for 2 minutes. This method affects the chemical properties of the photoresist, such as sensitivity, less, but is found to encounter difficulty when removing thick AMLs. 500nm thick AML cannot be completely removed by this method.

### 3.1.3 Future Improvements

Since the light passing through the AML and exposing the resist is mostly the near field component, only the very top layer of the resist would be exposed. In that case, using thinner resists and adjusting the development conditions accordingly, as shown in reference [3], would greatly improve the resist resolution as well as the line edge roughness in the final pattern in the resist. Furthermore, the use of an anti-reflection coating (ARC) would not be necessary because very little right will reach the bottom and reflect back anyway. However, features recorded in such thin resist would not be useful unless we can transfer the pattern to an underlying stack to obtain high aspect ratio features. A tri-layer transferable stack used for studies on near field optical patterning was proposed in reference [3].

## 3.2 The Absorption Modulation Layer (AML)

The key AMOL properties we are looking for were described in section 2.3.1. In this section, we investigate several photochromic materials according to the AML desirability specifications as an AML and summarize the lithographic results with each material system. The photochromic properties of each polymer were analyzed by spin coating on a glass slide, irradiating with a Hg lamp or laser light, and conducting UV-Vis spectroscopy. The choice of wavelengths was constrained by the available lines of the Hg lamp and laser sources we have. The photochromic parameters extracted from the photokinetic responses were successfully employed to explain the experimental results as described later in chapter 4.

### 3.2.1 The azobenzene polymer

The composition of the azobenzene polymer is shown in Fig. 3-1. The synthesis of the monomers and the polymerization process have been described in Ref.[22, 23]. The monomers is later polymerized with a large number of absorbing units per polymer chain, making the absolute absorbance in a 200nm film is as high as 2.4. With a polymer molecule, no matrix for spin-coating purpose is required. Upon exposure to $\lambda_1$=400 nm, the trans isomer undergoes a photoisomerization reaction forming the cis isomer. The reverse reaction is favored upon exposure to $\lambda_2$=532 nm. The cis isomer is also thermally unstable, slowly converting back to trans. The absorbances (at $\lambda_1$=400 nm) of the two isomers are markedly different as shown in Fig. 3-2. Figure 3-1 (a) shows the change in absorbance of 200 nm of the polymer measured at 405 nm upon exposure to 405 nm light at an intensity of 1.2 $mW/cm^2$. Figure 3-1 (b) shows the same when the sample was exposed to 20 $mW/cm^2$ light at 546 nm. The syntheses and UV-Vis measurements are done by Samuel W. Thomas III.

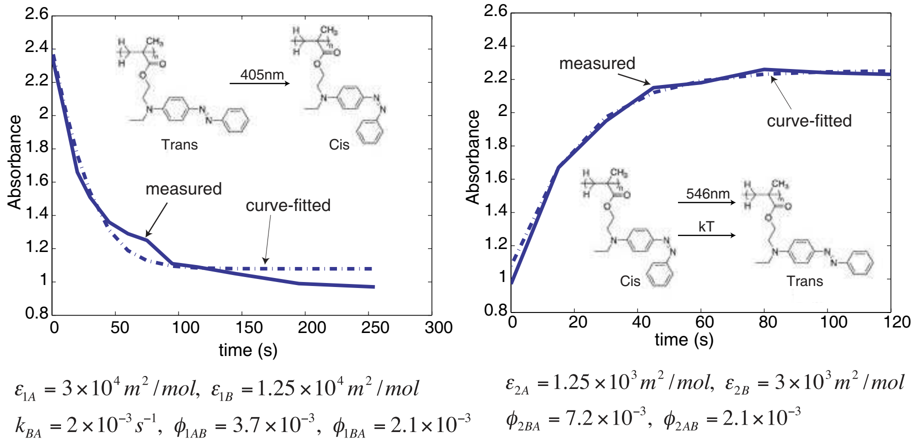

$\varepsilon_{1A} = 3\times10^4 m^2/mol,\ \varepsilon_{1B} = 1.25\times10^4 m^2/mol$

$k_{BA} = 2\times10^{-3} s^{-1},\ \phi_{1AB} = 3.7\times10^{-3},\ \phi_{1BA} = 2.1\times10^{-3}$

(a)

$\varepsilon_{2A} = 1.25\times10^3 m^2/mol,\ \varepsilon_{2B} = 3\times10^3 m^2/mol$

$\phi_{2BA} = 7.2\times10^{-3},\ \phi_{2AB} = 2.1\times10^{-3}$

(b)

Figure 3-1: Absorbance (at 405 nm) measured as a function of time, when a 200 nm photochromic layer was illuminated by (a) 1.2 $mW/cm^2$ light at 405 nm, and subsequently by (b) 20 $mW/cm^2$ light at 546 nm. The experimental data (solid) are overlaid with the simulation (dashed), which enables the extraction of the photochromic parameters.

Applying the photokinetic model described section 2.2.1 to the measured data, we extracted the material parameters for the azobenzene polymer. These parameters are listed in Fig. 3-1. The subscripts A and B refer to the trans and cis isomers, respectively, while the subscripts 1 and 2 refer to $\lambda_1$ and $\lambda_2$ respectively. The symbols $\epsilon$, $\phi$, and $k$ refer to the corresponding molar absorption coefficient, the quantum

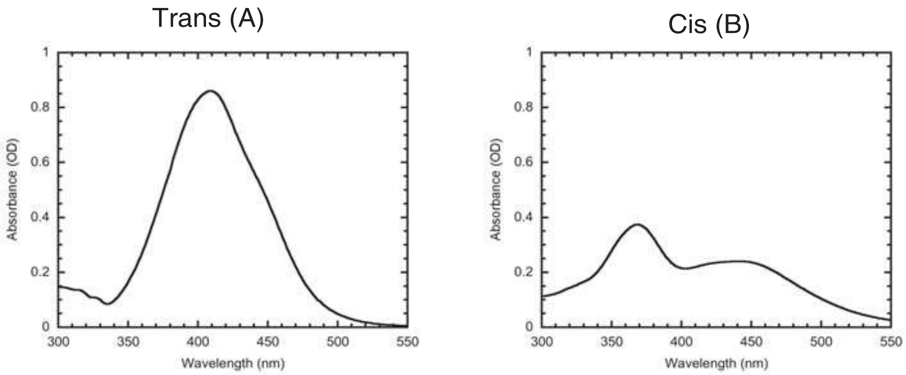

Figure 3-2: UV-Vis spectrum of the azobenzene monomer. The molecule shows an absorbance contrast about 4, which is one of the highest among the molecules we've tried. The fact that the peak absorbance of the trans form occurs close to the $\lambda_1$=400nm, and the absorbance drop close to 400nm for the cis form definitely helps the absorbance contrast. Although there is no absorption peak close to $\lambda_2$=532nm, the absorbance difference at $\lambda_2$ is still enough to bring the molecule back to the trans form with $\lambda_2$ light illumination.

efficiency and the thermal rate constant, respectively.

In summary, the azobenzene polymer exhibits high absorbance contrast, high absolute absorbance, and decent transition speed compared to the photoresist exposure speed (see chapter 4.) The transition wavelengths also match the laser wavelengths we have although $\lambda_2$ and $\lambda_1$ are still relatively close to each other, so many resists for 400nm light cannot be used because they are also exposed by 532nm light. However, the thermal instability of the azobenzene polymer imposes many limitations to the AMOL system as described in section 2.3.1, and, therefore, prompted us to search for other candidates for the AML.

### 3.2.2 The diarylethene

The composition and UV-Vis spectrum of the diarylethene is shown in Fig. 3-3. The way this molecule work as a photochromic material is described as follows. When the bond at the center between the two rings is open, the electrons of the two rings do not interact with each other much, creating two separate resonant cavities and an absorption peak at shorter wavelength. When the bond is closed, the entire molecule forms a resonant cavity and creates another absorption peak at longer wavelength. The molecules are synthesized by G. Zerbi's group from Dip. di Chimica, Materiali e Ingegneria Chimica "Giulio Natta" in Milan, Italy[24]. The actual diarylethene molecule we conducted experiment on has a slightly different spectrum, as shown in Fig. 3-4. The peak of the open form absorption is close to 300nm, and that of the closed form is close to 600nm. We used $\lambda_1$= 300nm filtered from a Hg lamp, and $\lambda_2$=633nm from a HeNe laser. The molecule was dissolved in a PMMA matrix for preliminary testing.

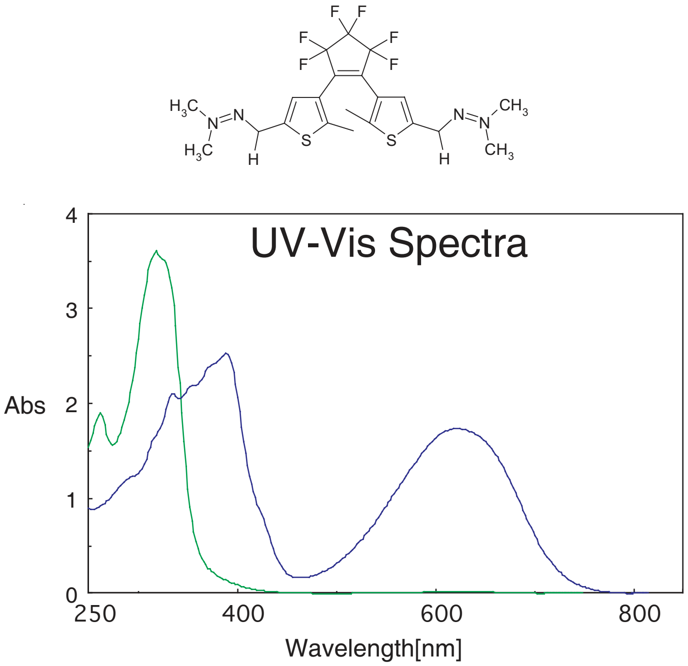

Figure 3-3: The molecular structure and the UV-Vis spectrum of the diarylethene.[24]

Although Fig. 3-4 shows the phototransitions at $\lambda_1$ and $\lambda_2$, we were not able to observe lithographic patterns in photoresists with diarylethene as the AML. This may be due to the low absolute absorbance at $\lambda_1$, resulting in low final image contrast in the resist. Compared to the 2.4 absorbance of the azobenzene polymer, the absorbance of the diarylethene film with the same thickness (200nm) is only 0.09. Even with a 500nm thick film as shown in Fig. 3-4, the peak absorbance is only about 0.27. Neither 200nm nor 500nm diarylethene were able to provide enough image contrast to be recorded in the underlying photoresist.

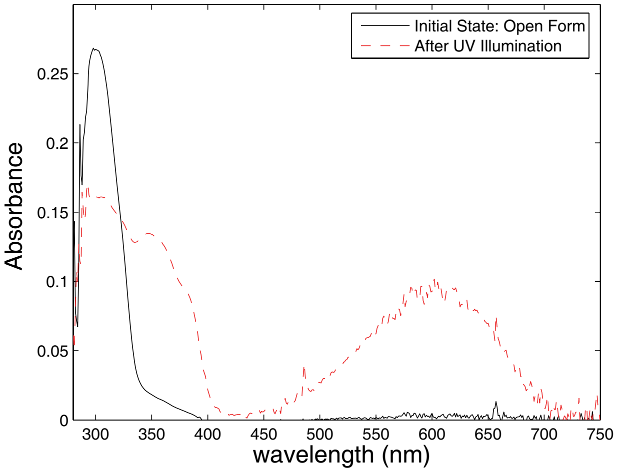

Figure 3-4: The UV-Vis spectrum of the diarylethene molecules used for AML. The diarylethene molecules were dissolved in PMMA and spun to 500nm to increase the signal to noise ratio for the UV-Vis measurement. It can be seen that the diarylethene is clearly not very absorbing, resulting in an insufficient image contrast for the AML. L1=300nm illumination was applied to for the transition from open form to close form, and l2=633nm illumination was applied for the reverse transition.

In summary, the diarylethene molecules exhibit thermal stability, and the two transition wavelengths are very far apart, making the choice of photoresist relatively easy. However, its low absolute absorbance and low absorbance contrast at the shorter transition wavelength limit its ability to provide high image contrast. Moreover, finding a coherent light source at 300nm wavelength is difficult. The coherence of the exposing wavelength is not extremely critical with the optical setup that will be described in chapter 4, but will be important for our ultimate goal of incorporating AMOL with the zone-plate array lithography (ZPAL) system. The wavelength where absorption peaks occur can be adjusted, and the absolute absorption may be increased through polymerization of the molecule, but the molecule we have is said to be close to its longest open form absorption already. Further modifications of this category of molecules are under investigation.

### 3.2.3 The fulgides

The composition of the furylfulgide is shown in Fig. 3-5. The way this molecule works is also by opening and closing of the bond between two resonant structures, similar to that of the diarylethene. The furylfulgide is purified so that the initial state before any illumination is 100% in its open form. The molecules are synthesized by Trisha L. Andrew. We used $\lambda_1 = 365$nm filtered from a Hg lamp, and $\lambda_2 = 532$nm from a laser. The fulgide molecule was dissolved in a PMMA matrix until saturation was reached at about 70% fulgide weight percentage to PMMA. The solvent of the PMMA was anisole. The measured UV-Vis spectrum is shown in Fig. 3-6. All fulgide films were spun to 200nm thickness.

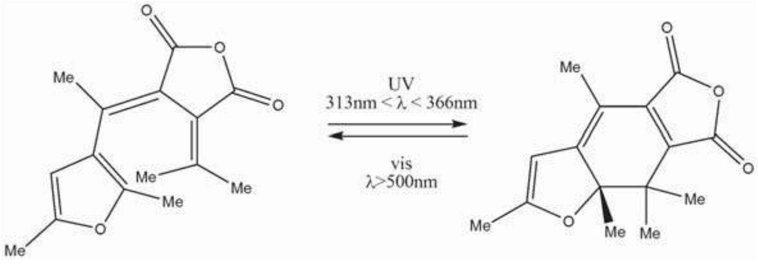

Figure 3-5: The molecular structure and transition wavelengths of the furylfulgide.

Fig. 3-6 (a) shows the UV-Vis spectrum for the photostationary states after $\lambda_1$ illumination and the spectrum after $\lambda_2$ illumination with dashed lines and dotted dashed lines, respectively. Photostationary states are reached when the spectrum does not change further with longer illumination. The absorbance at $\lambda_1$ decreased by a factor of 2 after only one photo-transition cycle, indicating that the fulgide molecules are degrading rapidly over the period of light illumination. Fig. 3-6 (b) shows the effect of only $\lambda_2$ illumination, which in theory, should not trigger any photo-transition, and the change of the spectrum over time. The fact that even $\lambda_2$ illumination bleached the fulgide molecules, and the dramatic decrease of the absorbance at $\lambda_1$ over time imply that the filgide is chemically unstable in the form of a film. Possible causes of degradation include contact with oxygen, which suggested the use of encapsulation. Fig. 3-6 (c) shows spectra measured under similar conditions to Fig. 3-6 (a),

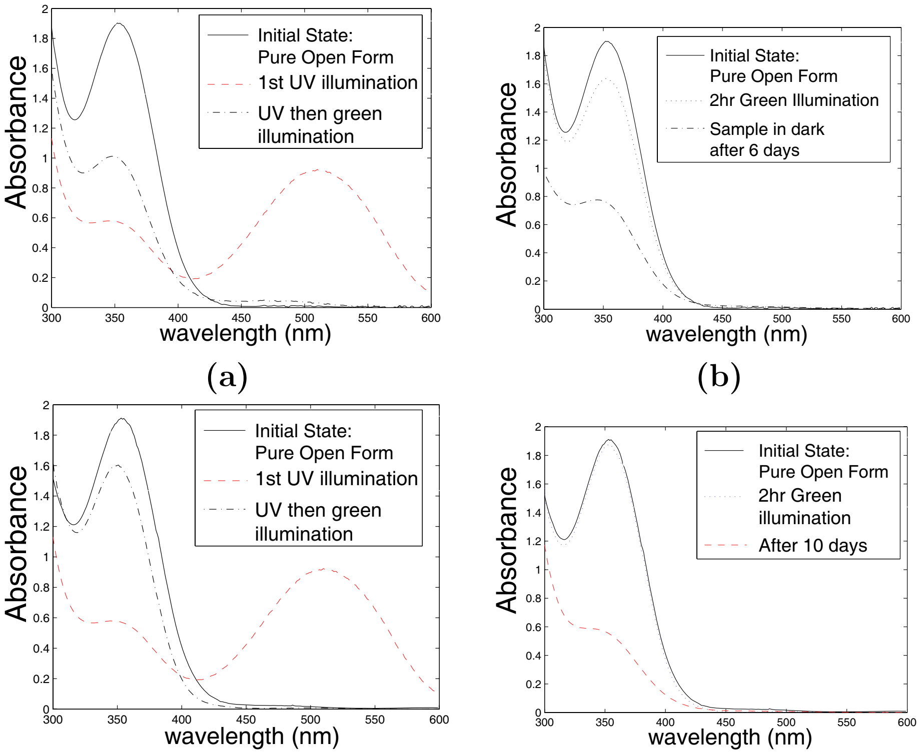

**(a)** **(b)**

**(c)** **(d)**

Figure 3-6: The UV-Vis spectrum of the furylfulgide. All fulgide samples were in PMMA and spun to 200nm thickness. (a) The UV-Vis spectrum for the photostationary states after $\lambda_1$ illumination and the spectrum after $\lambda_2$ illumination. The absorbance at $\lambda_1$ decreased by a factor of 2 after only one photo-transition cycle, indicating that the fulgide molecules are degrading rapidly over the period of light illumination. (b) The effect of only $\lambda_2$ illumination and the change of the spectrum over time. The great change in absorbance implies that fulgide is chemically unstable in the form of a film. (c) Spectra measured under similar conditions to (a), but with a 30nm PVA encapsulation layer spin-coated on the fulgide film. The high reversibility of the UV-Vis curve shows the PVA was protecting the fulgide molecules, increasing the photo-switching reversibility and lifetime of the molecules. (d) The spectrum after long $\lambda_2$ illumination almost did not affect the spectrum.

but with 30nm PVA spin-coated on the fulgide film. Although the molecules with UV-Vis spectrum shown by the dotted dashed line in Fig. 3-6 (c) has not reached its photostationary state, it already showed much higher absorbance compared to that in Fig. 3-6 (a). This shows that the PVA encapsulation was protecting the fulgide molecules, increasing the photo-switching reversibility and lifetime of the molecules. Fig. 3-6 (d) further confirmed this by showing that long $\lambda_2$ illumination almost did not affect the spectrum. However, the UV-Vis spectrum in Fig. 3-6 (d) of the PVA-protected samples after 10-day exposures to the ambient behaved similarly as the samples without PVA protection, suggesting that the oxygen in air gradually penetrates the PVA layer and affects the fulgide molecules.

In summary, the furylfulgide molecule exhibits high absolute absorbance at $\lambda_1$ and high absorbance contrast, about 3, but its poor chemical stability in contact with air leads to poor reversibility which is not acceptable for the purpose of AMOL. Although encapsulation greatly improved the reversibility of the film, the protection of the encapsulation layer did not last very long. Applying a thicker protection layer may slow down the degradation rate of the underlying fulgide. Nevertheless, It would be nice if the film works without additional protection. Modification of the side groups are under investigation at this point and showing promising results. One of the modified structures and its UV-Vis spectrum is shown in Fig. 3-7. The transition wavelengths of the fulgide are workable with a Hg lamp, but the molecule may suffer from lack of an available coherent light source.

## 3.3 Various Types of Photoresists

As described in section 2.3.2, the choice of photoresist to use in the stack depends on the AML property. In this section, we describe the properties of various types of photoresists and compare their strengths and weaknesses for application to the AMOL system with the azobezene polymer AML described in section 3.2.1.

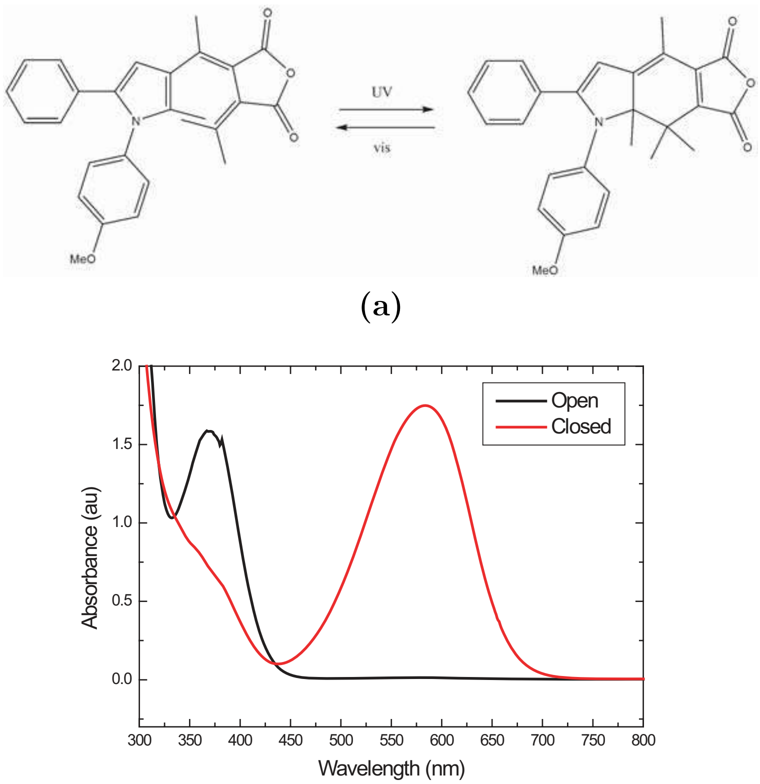

**(a)**

**(b)**

Figure 3-7: The structure and UV-Vis spectrum of the OMePyrrolefulgide

### 3.3.1 PFI-88 and S1813

PFI-88 from Sumitomo Chemical Co., Japan, is a 2-Heptanone based i-line (365nm) resist, while S1813 is a g-line (436nm) resist from Shipley, USA. The developers for the two resists are CD-26 and MF123, respectively. No post-exposure bake is required for either resists. Both are positive resists that undergo chain scission when illuminated with light. Both resists posses a relatively high sensitivity at $\lambda$=400nm, which is the $\lambda_1$ wavelength for the azobenzene AML. However, since the sensitivity to 532nm (green) light ($\lambda_2$=532nm for the azobenzene AML) is also relatively high, these two resist could not be used as the recording layer for AMOL with the azobenzene AML. Instead, the two resists were used for recording and characterization of the optical properties of the patterns created in the green beam.

### 3.3.2 PS-4 (Tokyo OHKA Kogyo Co., Ltd., Japan)

PS-4 is a chemically-amplified resist from Tokyo OHKA Kogyo Co., Japan. It contains a polymerization backbone and an i-line (356nm) sensitive photo acid generator(alpha-methyloxyimino-p-methoxyphenylacetonytolyl). PS-4 is a negative resist that was processed with a post-exposure bake at 115 °Cfor 90 seconds to initiate the cross linking of the exposed photoresist. Only the unexposed regions are removed upon development. The developer is CD-26 (0.26N tetramethylammonium hydroxide, Shipley, USA). The PS-4 resist exhibits high spatial resolution at a thickness of 150nm, but does not work as well when we tried to thin the resist down ourselves with Propylene Glycol Methyl Ether Acetate (PGMEA) to obtain thinner films (90nm and 50nm films). It was found that the sensitivity to lights drops dramatically if we process the resist with the same pre-bake conditions. Longer pre-bake was shown to help increase the sensitivity, but the line edge roughness and final image contrast in the resist are still not as good compared to those in 150nm thick film. In addition to the difficulty of thinning the resist, negative resists are by nature inappropriate for near field exposures since the near field components mostly expose only the top of the resist. The PS-4 resist has a good sensitivity at 400nm, while having very low sensitivity at 532nm, making it the first resist we used for the recording stack to demonstrate AMOL. Nevertheless, its sensitivity to green becomes a problem when we attempt to increase the $\lambda_2$ to $\lambda_1$ ratio because the high dose at $\lambda_2$ exposes the resist before $\lambda_1$ does.

### 3.3.3 IBM highEA Resist

The IBM highEA resist is a proprietary positive resist developed at IBM for RD purpose only. The resist is a deep-ultra violet (193 nm) photoresist mixed with a photoinitiator to generate sensitivity at 400 nm. This was accomplished through the addition of an electron transfer photosensitizing dye (2-ethyl, 9,10 dimethoxyanthracene) to a commercial ArF photoresist (JSR AR1863J). A post-exposure bake at 125 ℃ for 90 seconds followed by development in CD-26 was applied after exposing the resist. Although this photoresist formulation exhibited high sensitivity to $\lambda_1$=400nm and very low sensitivity to $\lambda_2$=532 nm, the resist properties were optimized for 170nm thick films and also suffered from dramatic sensitivity decrease with the decrease of film thickness to about 50nm. This could be caused by contamination at the surface of the chemically amplified resist, which is still under investigation.

# Chapter 4

# Generation of a 2D Optical Node and Lithography Results

In this chapter, we demonstrate the one-dimensional equivalent of the absorbance modulation optical lithography (AMOL) technique. In particular, we exposed fringes formed by two-beam interference at $\lambda_2 = 532$ nm, and a uniform beam at $\lambda_1 = 400$ nm to the stack described in chapter 3 with the azobenzene absorbance-modulation layer (AML). Only the transmitted light at $\lambda_1 = 400$ nm exposes the underlying photoresist layer.

## 4.1 The Lloyd's Mirror Setup

The optical setup consisted of a Lloyd's mirror configuration, as depicted in Fig. 4-1. The output of a 532 nm laser was expanded and collimated, before impinging on the Lloyd's mirror and the substrate, resulting in a standing-wave pattern on the surface of the substrate. Light from a 400 nm laser was made coincident with the first beam by a polarizing beam splitter. A beam block was used to ensure that no 400 nm light was incident on the Lloyd's mirror. As a result, the substrate was illuminated by a standing wave at $\lambda_2 = 532$ nm, and a uniform beam at $\lambda_1 = 400$ nm. The beam profiles near the substrate were measured and the intensities near the optical axis at 400 nm and 532 nm were estimated as 1.7 mW/cm$^2$ and 6.4 mW/cm$^2$, respectively.

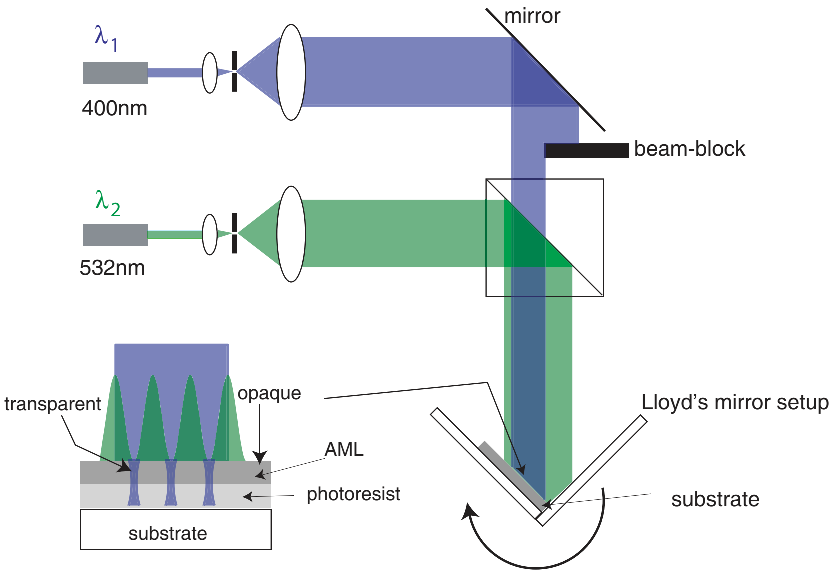

Figure 4-1: Schematic of Lloyd's mirror setup for AMOL. The standing-wave illumination at $\lambda_2$ creates local apertures for $\lambda_1$, through which the underlying photoresist is exposed.

## 4.2 Single Exposures

### 4.2.1 Exposures on PS-4 Resist

Scanning-electron micrographs of typical exposed patterns are shown in Figs. 4-2 (a) and 4-2 (b). The period of the lines is identical to the period of the standing wave at $\lambda_2$, and it may be adjusted by the angle between the incident beam and the Lloyd's mirror. Since PS-4 has very low sensitivity to $\lambda_2 = 532$ nm, the exposure in this case is exclusively due to the localized light fields at $\lambda_1 = 400$ nm generated by the absorbance modulation in the AML. This situation is analogous to contact photolithography with the dynamically formed aperture in the AML in place of the photomask. The lines in Fig. 4-2 (b) were formed near the center of the 400 nm beam with an exposure time of about 90 min, whereas those in Fig. 4-2 (a) were formed at the far edges of the blue beam (where the intensity is significantly lower) with an exposure time of about 240 min. The smallest linewidth that we were able to resolve was about 100 nm. This was primarily limited by the thickness of the PS-4 photoresist (150 nm). The significant line-edge roughness evident in Fig. 4-2 (a) is likely due to the underexposure of the chemically-amplified photoresist.

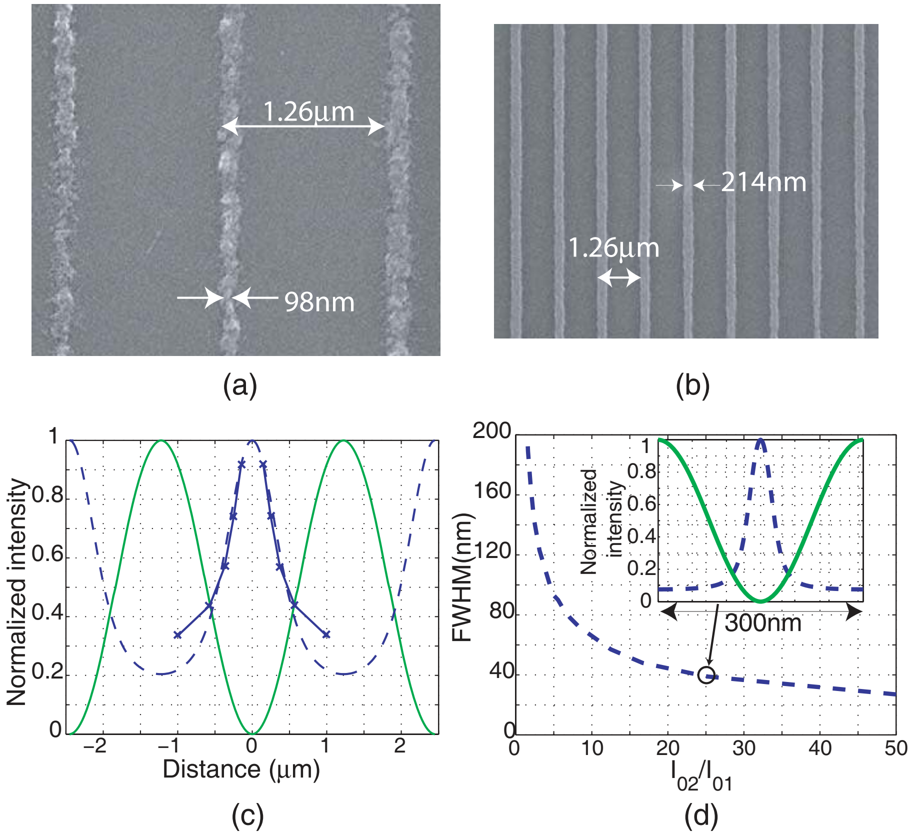

(a) (b) (c) (d)

Figure 4-2: (a),(b) Scanning electron micrographs of lines exposed in negative photoresist. The average linewidth of the middle line in Fig. 4-2(a) is about 117 nm. The period of the lines is determined by $\lambda_2$ and the angle in the Lloyd's mirror setup. (c) Light intensity distribution of the localized fields underneath the AML for a standing-wave period of 2.45 $\mu$m. The simulated data is shown with dashed lines. The experimental data is overlaid (solid line) for comparison. (d) Calculated FWHM as a function of $I_{02}/I_{01}$ for a standing-wave period of 300 nm. The parameters of the AML listed in Fig. 3-1 were used in all the simulations.[25]

### 4.2.2 Exposures on IBM highEA Resist

As described in section 3.3.3, the IBM highEA resist has several advantages over PS-4. We, therefore, continued the study on the line-spread function (LSF) compression with smaller grating period with the IBM highEA resist. The thickness of the IBM highEA resist used here is 170nm. The Lloyd's mirror is the as shown in Fig. 4-1 with similar power ratio at the center of the beams. The period of the gratings in this case is 1.6 $\mu$m.

In addition to mapping out the LSF at one single position and comparing it to theory, the LSFs at various positions are measured and compared qualitatively. The comparison could not be made quantitatively due to the lack of information on the exact intensity distributions of the beams, so the ratios of the green and blue beams at each position on the sample is unknown. However, with the information of the average intensity ratio to the two beams and by matching experimental data to simulation, we were able to correlate the change of LSFs to the change in $I_{02}/I_{01}$ ratios. Fig. 4-3 shows two sets of LSFs with one broader than the other. The one with sharper LSF was measured closer to the edge. This could be caused by several factors. In the setting of this set of experiments, the blue beam is relatively uniform in the region of measurement, while the green beam intensity decays quite a bit as we move away from the edge. Therefore, the green to blue beam intensity ratio ($I_{02}/I_{01}$) becomes smaller as we get farther from the edge, resulting in the broadening of the LSF. This hypothesis is supported by Simulation results, showing the LSF close to

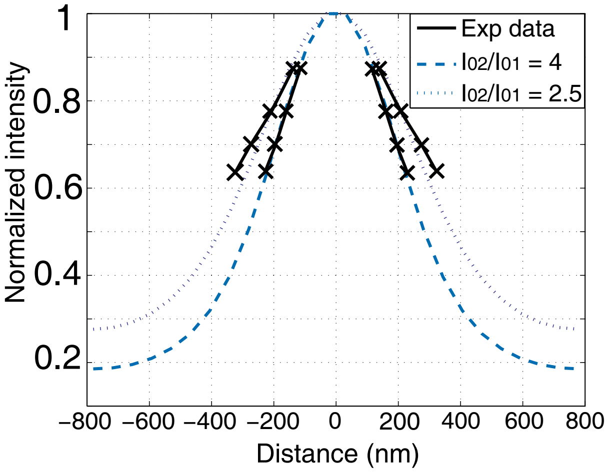

Figure 4-3: LSF for single exposures on highEA resist at different positions. Black solid lines are experimental data of LSF measurements at two different positions on the sample. The exact $I_{02}/I_{01}$ ratios at these positions were unknown, but the average $I_{02}/I_{01}$ value is about 4. Simulation results with reasonable $I_{02}/I_{01}$ ratios matches the experimental data well, supporting the hypothesis that the difference in LSF could be caused by the change of $I_{02}/I_{01}$ ratio.

the edge matches well with the $I_{02}/I_{01} = 4$ LSF, while the one farther from the edge corresponds to the $I_{02}/I_{01} = 2.5$ case. It is also possible that the contrast of the green gratings decays away from the edge due to the short coherent length (only a few millimeters) of the green light laser used, As shown in section 2.3.3. However, because the $I_{02}/I_{01}$ used in this case is relatively low, introducing background affects the background level of the LSF, but not shape of the main lobe.

## 4.3 Multiple Exposures

In the semiconductor industry, the scaling of lithographic features has been enabled by sources of deep-UV wavelengths as well as significant improvements in the quality of the imaging systems. The technological problems associated with short-wavelength sources[26] have forced the need for novel techniques to extend the resolution of tools to meet future lithographic requirements. This has driven the development of immersion-lithography tools, where a medium of high refractive index is inserted in between the last optical element and the substrate, to increase resolution[27]. However, absorption associated with increased refractive index places practical limits on the achievable resolution.

A technique of multiple exposures was proposed to overcome this limit[28]. In this technique, patterns of readily achievable spatial periods are exposed sequentially and with appropriate spatial-phase shifts[29]. Each exposure is followed by a development to define the pattern in the photoresist as well as an etch to transfer the pattern into an underlying sacrificial layer. Then, another layer of photoresist is spun on for the next exposure. Once all the exposures are completed, the sacrificial layer is used as an etch mask to transfer the final pattern into the substrate. Diffraction limits the spatial period of the patterns that can be printed. However, the size of a printed feature (e.g., the “duty cycle” of a periodic pattern) can be made much smaller through nonlinearities introduced by the photoresist or subsequent etching steps. Thus, patterns of high spatial frequencies (and high resolution) are enabled at the expense of a slower and more complicated process. In this section, we describe an alternative technique that utilizes absorbance modulation to introduce the requisite nonlinearities and enables multiple exposures in a single resist layer without intervening process steps.

### 4.3.1 Process Flow

We performed two sequential exposures at two different angles of the Lloyd's mirror, which resulted in interleaved exposed lines in the photoresist. The Lloyd's mirror setup can be rotated about the hinge line, where the mirror is attached to the substrate holder. Rotating the setup with respect to the illumination allows the period of the standing wave at $\lambda_2$ to be changed. In this set of experiments, the 170nm IBM highEA resist was used for the photoresist layer. The experimental procedure is illustrated in Fig. 4-4. After the first exposure, the 400nm beam is turned off and the Lloyd's mirror setup rotated to the second angle. The AML is exposed to the 532nm for approximately 20 minutes to ensure that the absorbance is recovered to the initial value. After turning on the 400nm beam and conducting the second exposure, the AML stack is processed with the standard AML removal process with trichloroethylene, the proper development process for IBM highEA resists, and sputter-coated with a thin Au/Pd alloy before inspection in a scanning-electron microscope.

### 4.3.2 Spatial-frequency Multiplying with AMOL

Scanning-electron micrographs of patterns in photoresist after a double exposure and development are shown in Fig. 4-5. In Fig. 4-5 (a) the center line was exposed during the first exposure, while the surrounding two lines were exposed during the subsequent second exposure. The periods of the standing wave at $\lambda_2$ for the two exposures were 1.733 $\mu$m and 2.08 $\mu$m, respectively. As a result of the double exposure, a line-space pattern of approximately 800nm period was formed locally, effectively increasing the spatial frequency of the printed pattern by a factor of two. In Fig. 4-5 (b), the printed pattern is compared to a simulation of the double exposure. The simulated pattern was calculated by adding the two separate exposures. It is clear from the simulation

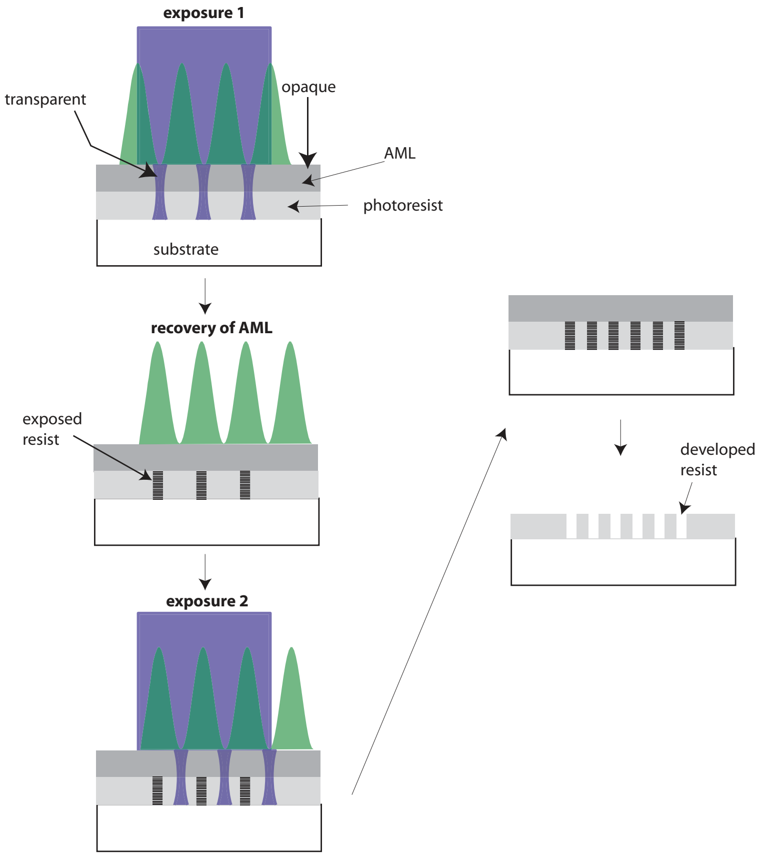

Figure 4-4: Schematic illustrating the double-exposure technique. The first exposure is conducted with a period, $P_1$ of the standing wave at $\lambda_2$. The period is changed to $P_2$ for the second exposure. A long exposure in between the two exposures with only $\lambda_2$ ensures that the AML recovers to its original opaque state.

that the nonlinearity introduced by absorbance modulation generates spatial frequencies in the printed pattern much higher than those present in the incident standing wave.

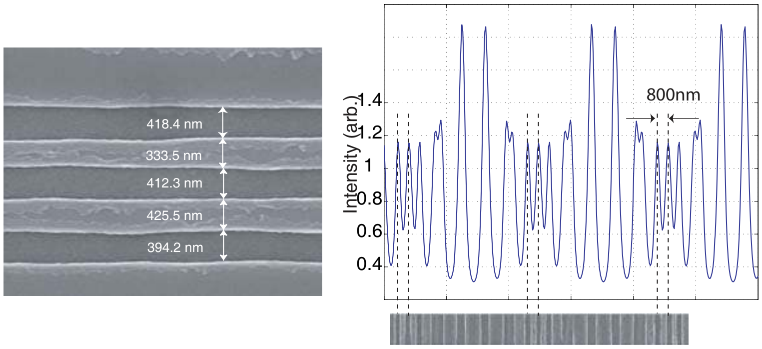

(a)

(b)

Figure 4-5: Spatial-frequency multiplication by double exposure. The first exposure was conducted at a period of the standing wave at $\lambda_2$ of 1.733 $\mu$m, and the period of the second exposure was 2.08 $\mu$m. (a) Scanning-electron micrograph of 3 lines. (b) The aerial image of the double-exposure pattern simulated by adding the two individual exposure patterns. Each exposure pattern was simulated using the model described in section 2.2.1[15]. Note the agreement of the location of the fringes with the scanning-electron micrograph of the exposed pattern.

It was pointed out earlier in section 2.2.1 that the width of the LSF of $\lambda_1$ transmitted through the AML can be decreased by scaling the ratio of the intensities at the two wavelengths. Thus, absorbance modulation provides a means to overcome the far-field diffraction limit and pattern sub-wavelength features. Since the absorbance-modulation layer can be completely reversed to its initial state after each exposure, the history of prior exposures is completely removed. Combining these two unique properties, it is possible to apply multiple exposures to generate dense, sub-wavelength features. Since the absorbance of the AML is reversible via exposure to $\lambda_2$, the exposures can be repeated as many times as necessary without ever removing the substrate from the exposure tool. Experimental results shown in this section demonstrate a two-fold increase in local spatial frequency. Extension of this technique to multiple exposures and higher nonlinearities should enable the creation of nanoscale periodic patterns using simple far-field optics.

### 4.3.3 Controlled Experiment with PFI-88 Resist

The nonlinearity introduced by the AML is crucial for the spatial-frequency-multiplication technique. In order to confirm this, we performed double exposures on substrates without the AML using a conventional Lloyd's-mirror interferometer. The Lloyd's mirror was rotated such that the periods of the standing waves for the two exposures were 1.6 $\mu$m and 1.95 $\mu$m. The exposures were performed at $\lambda = 325$nm on silicon wafers coated with 200nm ARC and 100nm of photoresist (PFI-88). Scanning-electron micrographs in Figs. 4-6 (a), and (b) show the developed resist for exposure doses for exposures of 15s, and 20s, respectively. Characteristic beat spatial frequencies are clearly visible and agree well with the simulated aerial image (see Fig. 4-6 (c).) However, since the two exposures add linearly in the photoresist, the spatial frequency in the final pattern is still limited to the highest spatial frequency in the component standing waves. No spatial frequency multiplication is possible without the nonlinearity introduced via absorbance modulation.

## 4.4 Limitations of the Lloyd's Mirror Setup

In order to characterize the performance of the Lloyd's mirror setup, we take the line-spread function (LSF) mapped out in the IBM highEA resist shown in section 4.2.2 as an example. Figure 4-7(a) shows the experimental measurements of the LSF as well as the theoretical values. A noise level of 3%(of the peak) in the node of the standing wave was assumed, and was experimentally verified by separate photoresist exposures. The ratio of the intensities between the two wavelengths was about 4. We observed that the range of linewidths that could be experimentally obtained was limited. This can be explained by studying the inverse of the slope of the theoretical LSF as a function of the spatial coordinate, shown in Fig. 4-7(b). Beyond a small range of linewidths between 250nm and 600nm the inverse slope diverges. Since the exposure latitude is directly proportional to the slope of the LSF, this limits our ability to reliably map the LSF to those linewidths. This limitation is not inherent to AMOL, but to some limitations of our particular Lloyd's mirror setup, which will

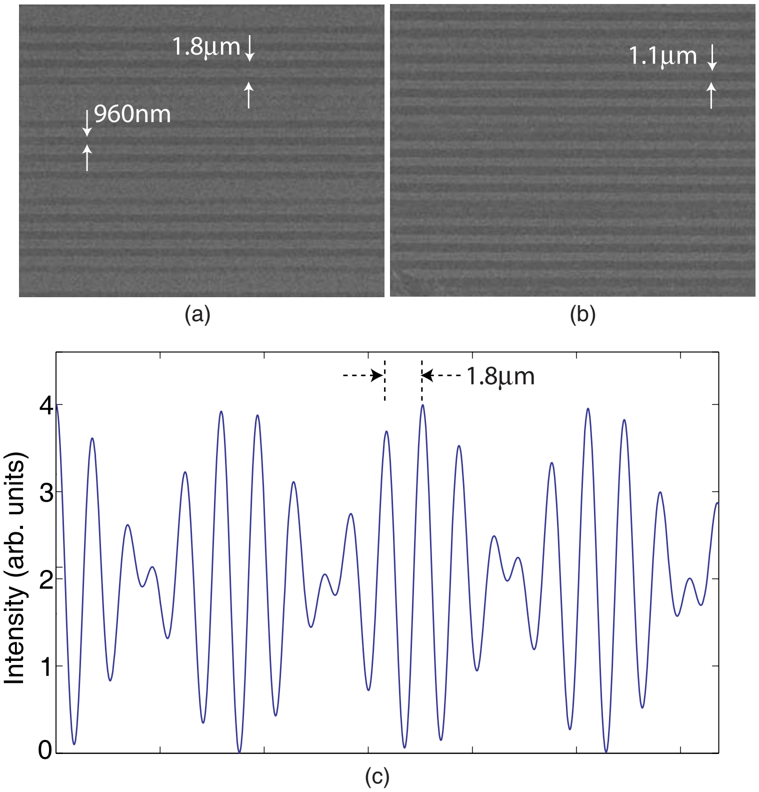

(a)

(b)

(c)

Figure 4-6: Double exposure without using an AML. Scanning-electron micrographs of developed photoresist for exposure doses of (a) 15s and (b) 20s. The double exposure was performed in a Lloyd's mirror setup at an illumination wavelength of 325nm. The periods of the two exposures were 1.6 $\mu$m and 1.95 $\mu$m. Note that the highest spatial frequency in the double exposure corresponds only to an average of those of the two individual exposures. (c) Simulated aerial image of the double-exposure pattern without the AML. Spatial-frequency multiplication is not possible in this case.

be discussed below.

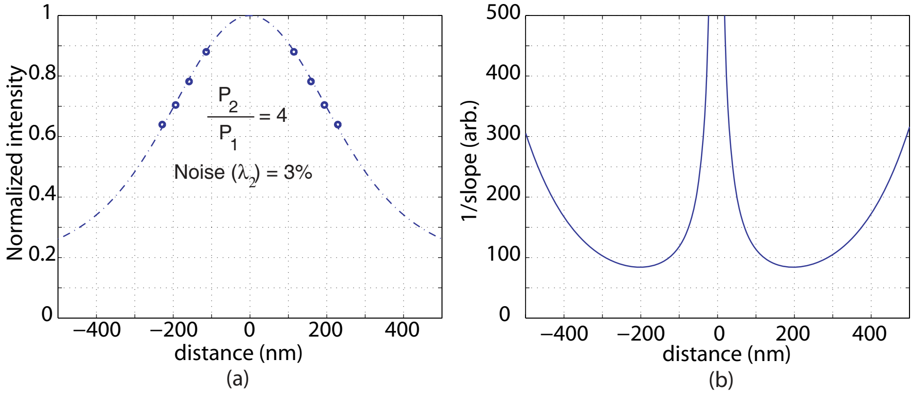

Figure 4-7: Mapping the line-spread function (LSF). (a) The dashed line is the simulated LSF of the transmitted light at $\lambda_1$, when the period of the $\lambda_2$ standing wave is 1.6 $\mu$m. A noise level of 3%(of the peak) in the node of the standing wave was assumed. The ratio of the intensities between the two wavelengths was about 4. The parameters of the AML are those of the azobenzene polymer, described in section 3.2.1. The circles are experimental values. (b) The inverse slope of the simulated LSF as a function of the spatial coordinate. Note that the slope begins to diverge except for a small region of linewidths between 250nm and 600nm. This limits the exposure latitude in our experiments. Simulation is done by Rajesh Menon.

### 4.4.1 Contrast of the Green Gratings

As discussed earlier in chapter 2.3.3, the node quality of $\lambda_2$ is crucial to the final resolution in the patterns created by AMOL, especially when the $I_{02}/I_{01}$ is high. However, the coherence length of our green beam laser is only of the order of several millimeters. Therefore, the area where the green grating contrast is high enough to demonstrate the high resolution capability of AMOL is very small and becomes even smaller as we decrease the period of the gratings. In addition, since the mirror in the Lloyd's mirror is only a wafer coated with electron-beam-evaporated aluminum, its imperfect reflectivity and scattering from scratches also decreases the contrast of the grating. Vibration problems of the sample was also found to affect the contrast, but was greatly reduced by using a vacuum chuck at the stage to hold the sample.

### 4.4.2 Lack of Translational Accuracy and Focusing Ability

The Lloyd's mirror setup has an obvious disadvantage lacking translational flexibility and accuracy. That's exactly why we could only conduct multi-exposure experiments by changing the period of the Lloyd's mirror. Furthermore, since the Lloyd's mirror does not focus the incident beam, the throughput of this lithography system relies solely on the incident beam powers. We, therefore, need to compromise between low $\lambda_1$ beam power to achieve large $\lambda_2$ to $\lambda_1$ power ratio and high $\lambda_1$ beam power to avoid long exposures. Nevertheless, the Lloyd's mirror setup is relatively simple, and the line exposures do not require stage scanning. Therefore, the Lloyd's mirror setup is still useful, especially for the material search process for the AML, to demonstrate the feasibility of AMOL. For our final goal of patterning arbitrary patterns with ultimate resolution of AMOL, with reasonable throughput, we will need an optical element that creates a focused ring-shaped beam profile with a high quality node at the center. This will be discussed in the next chapter.

# Chapter 5

# Generation of an Optical Node

Focused beams of light with central nulls are essential for a variety of applications including particle manipulation [30], fluorescence microscopy [31], and deep sub-wavelength lithography [15, 25, 32]. In all these applications, the intensity of the light at the central null should be minimized. Imposing an on-axis phase singularity on a plane wave will generate a beam with a central null. We investigated two approaches to fabricating spiral-phase diffractive elements in polymethyl methacrylate (PMMA) using scanning-electron-beam lithography (SEBL). The first device was a spiral-phase plate (SPP) [33], fabricated using grayscale SEBL; the other was a binary spiral-zone plate (SZP) [34].

## 5.1 Basic Principles

### 5.1.1 Property of Diffractive Optical Devices

When a light wave is delayed by one wavelength in light path, corresponding to a $2\pi$ phase lag, no difference to the original wave can be found. Eq. 5.1 shows this relation mathematically, where $U(x)$ is the light wave, and $A(x)$ is the amplitude function.

$$U(x,\phi) = A_0(x)e^{i\phi} = A_0(x)e^{i(\phi+2\pi)} = U(x,\phi+2\pi) \tag{5.1}$$

The phase difference that a light encounters between traveling in a material with index of refraction $n$ and in air is $\frac{2\pi\cdot(n-1)\cdot\Delta l}{\lambda}$,where $\Delta l$ is the physical distance that the light travels in the material, and $\lambda$ is the wavelength of the light. In Eq. 5.1, we find that taking the $2\pi$ modulus of the phase $\phi$ does not change the light wave. Therefore, the maximum phase difference a diffractive optics needs to provide is $2\pi$, so the maximum $\Delta l$ , which reflects the maximum thickness of the device, is only

$$\Delta l_{max} = \frac{\lambda}{(n-1)} \tag{5.2}$$

Figure 5-1 illustrates this idea by showing two examples of such diffractive optical devices: a prism and a lens.

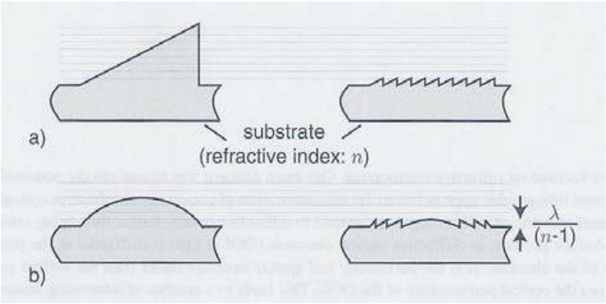

Figure 5-1: The blazing of (a) a prism and (b) a lens, resulting in a reduced thickness of the elements.[35]

Features on thin devices usually have smaller aspect ratio and are, therefore, easier to fabricate. However, a different type of fabrication difficulty accompanies this nice property. In the case of Fig. 5-1 (b), the feature height is discontinuous whenever its height reaches $\Delta l_{max}$ , but an ideal step with a finite difference in height and zero lateral width is hard to achieve. Good control in lateral displacement will result in a better approximation to the ideal design. Therefore, this method, which maps the phases of a diffractive optical device into the $[0, 2\pi]$ region, requires relatively high lateral resolution to minimize fabrication errors at each step. These fabrication errors will contribute to the loss of efficiency and dispersion of the device.

### 5.1.2 Different quantization schemes for diffractive lenses

Besides the difficulty in fabricating sharp steps, quantization is also an important issue in grayscale fabrication. Due to the resolution limit, dose-control-precision limit, and the way current scanning-e-beam lithography (SEBL) systems are programmed, we must apply some kind of quantization on the designed dose pattern. Nevertheless, quantization methods are not unique. Three different quantization schemes are shown in Figure 5-2, all applicable to implementing the same diffractive lens.

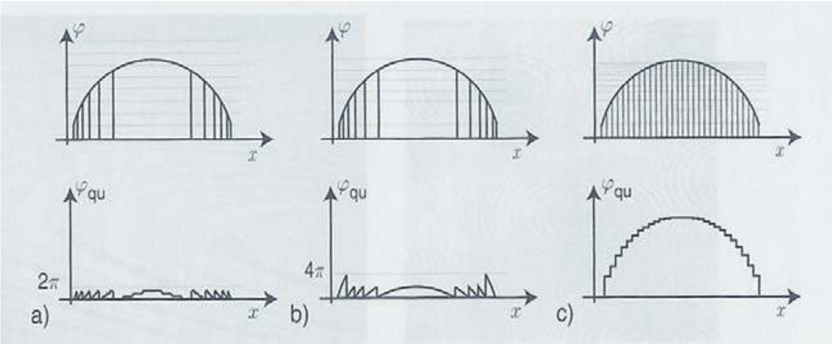

Figure 5-2: Different quantization schemes for diffractive lenses: (a) conventional quantization based on the Fresnel zones; (b) superzone concept to increase the aperture of diffractive lenses; (c) constant pixel size quantization.[35]

In Fig. 5-2 (a), the phase is first quantized to a phase depth of $2\pi$ and then approximated with discrete steps of equal phase depth. Fig. 5-2 (b) illustrate a method that prevents the period of the outer zone itself from becoming too small, but suffers the same quantization limit as Fig. 5-2 (a) because the width of each quantization step must decrease towards the outer zones to preserve the equal phase quantization and eventually reaches the resolution limit of the lithography system. Fig. 5-2 (c) utilizes a different quantization, which keeps the pixel size constant over the entire element. The phase steps are much lower in the central area than in the outer zones of the lens. Therefore, the efficiency of the inner zones is also higher in this case, resulting in undesirable diffractive effects.

### 5.1.3 zone plates (FZPs) and its grayscale limit

In this section, we use the FZP as an example to illustrate the effect of level quantization. Figure 5-3 shows the basic structure of a Fresnel zone plate.

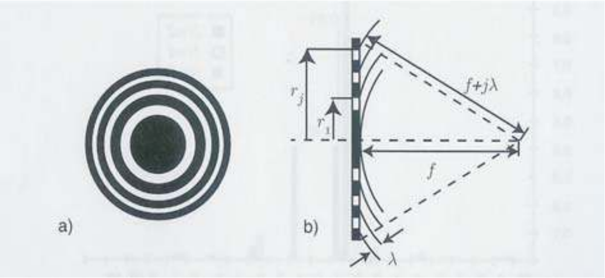

Figure 5-3: Arrangement of the annular rings in Fresnel lenses: (a) texture of the Fresnel zone plate; (b) optical path differences between light rays from different zones.[35]

In FZPs, the ring system consist of diffracting binary phase or amplitude structures that allows diffracted light waves with constructive phases to reach a common focal point. In the case of binary amplitude FZPs, as shown in Figu. 5-3 (b), the condition of the radius of the open zone, $r$, can be described as:

$$r_j^2 + f^2 = (f + j\lambda)^2, j \in N \tag{5.3}$$

where $r_j$ is the radius of the $j$-th opening on the FZP, $\lambda$ is the wavelength of the incident light, and $f$ is the focal length of the FZP. Only those rays with phase differences of multiples of $2\pi$ reach the focal point, so the FZP acts as a focusing lens. However, the binary amplitude FZP has several drawbacks, such as its low focusing efficiency and large background noise. This low efficiency can be seen from the fact that most parts of the incident light are blocked. Therefore, the binary phase FZPs, instead of blocking the portions of light that are out of phase, introduce a $\pi$ phase shift on the portions of light that are blocked by the binary amplitude FZPs. In fact, this idea can be generalized to achieve the grayscale limit of FZPs.

Let N be the number of phase level in the FZP. For example, N=1 corresponds to a binary amplitude FZP, N=2 corresponds to a binary phase FZP, and N=$\infty$ corresponds to an ideal blazed FZP obtained by phase quantization of an ideal lens, as described in 5.1.2. It can be calculated quantitatively how the efficiency rises as N increases, using a staircases phase profile approximation under the paraxial limit.[35] The result is plotted in Figure 5-4. Note that although this was derived for the paraxial case, the result also applies for diffractive lenses with small f-numbers.[35] We can see from Fig. 5-4 that using only 8 phase levels provides efficiency as high as 95%.

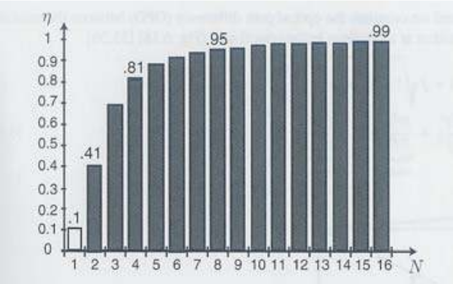

Figure 5-4: Efficiency of diffractive lenses at the focal spot vs. the number of phase levels. Here N=1 refer to an amplitude Fresnel zone plate. [35]

### 5.1.4 Two different approaches to fabricating spiral-phase diffractive elements

#### The spiral phase plate (SPP)

A spiral phase plate is also called an optical vortex. "In an optical vortex, the wavefront spirals like a corkscrew, rather than forming planes or spheres. Since any nonzero optical amplitude must have a well-defined phase, the axis of a vortex is always dark," as described in reference [21]. The phase distribution of a spiral phase plate is illustrated in Fig. 5-5 (a). The maximum phase step required for an SPP is $2\pi$, and the depth, $d$ follows $d = \Delta l_{max}\phi/(2\pi)$, where $\phi$ is the azimuthal angle, and $\Delta l_{max}$ corresponds to the thickness of a phase step that provides $2\pi$ phase shift, as defined in Eg. 5.2.

**The spiral zone plate (SZP)**

A focused spot with a central node is also generated by a binary spiral zone plate (SZP). An SZP, as shown in Fig. 5-5 (b), is generated when an azimuthal phase variation is imprinted on a conventional Fresnel zone plate. A method of generating optical phase singularities using computer-generated binary holograms was proposed in 1991 [36]. As described in 5.1.3, a computer-generated binary hologram is analogous to the N=1 case for FZP, while a binary-phase spiral zone plate corresponds to the N=2 case. Although binary-phase elements provide a first-order focusing efficiency of only about 40%, binary-element fabrication techniques are more robust.

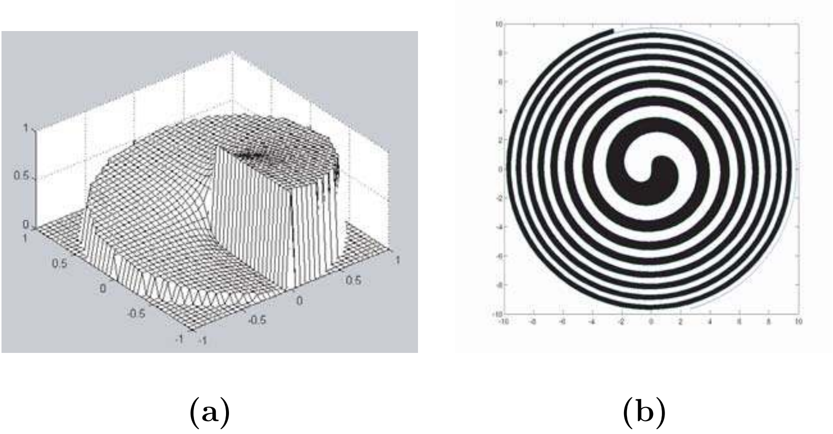

(a) (b)

Figure 5-5: The phase distribution of (a) the spiral phase plate, and (b) the binary spiral zone plate (black represents a $\pi$ phase shift).

## 5.2 Spiral Phase Plates

### 5.2.1 Past Work and Choice of Resist and Developer

In the past, SPPs were either fabricated in quartz using photolithography with an 8-step, aligned expose-and-etch procedure [33], or in low-contrast negative X AR-N 7220 e-beam resist using 32-level grayscale SEBL [37]. In both cases the phase discretization introduces background noise into the focused beam, causing the intensity of the central null to be non-zero. Furthermore, the first case suffers from errors introduced during multi-level alignment. We investigated an approach using grayscale SEBL to fabricate the SPP in a selected electron beam resist with a single lithography step, resulting in a continuous variation in phase.

### Three e-beam resist candidates

In order to provide the $2\pi$ phase shift required for SPP, we need to select an e-beam resist that is reasonably transparent at $\lambda_1$ and $\lambda_2$, gives good physical properties, such as thickness and rigidity, and is easy to process. Previous research has shown promising results of blazed structure lithography with e-beam using HSQ, PMMA, and SU-8 as e-beam resists. [1] Among the three, PMMA is insensitive to contamination, resulting in a more flexible and robust process. However, PMMA has the drawback of being opaque at deep UV wavelength, implying that these lenses in PMMA are not compatible with wavelength scale down. HSQ has a large transmission bandwidth down to deep UV and produces rigid structures after development, but is very sensitive to contamination and, therefore, more difficult to process. SU-8 has a relatively high index of refraction, so requires less physical thickness to produce the same phase shift. This property is beneficial because flatter structures are usually easier to fabricate. SU-8 also remained hard after development and can be used for blazed lithography with UV light. Nevertheless, SU-8 is a chemically amplifying photoresist, which is extremely sensitive to contamination. It also contaminates the processing environment. Moreover, most SU-8 studies focus on thicker devices in micro-fabrication, which may not be applicable to the SPP fabrication. We decided to fabricate the SPP in PMMA because for our current AMOL system, PMMA is transparent to both $\lambda_1$ and $\lambda_2$.

### Previous work on PMMA grayscale lithography processes

T. Fujita, et al. showed solid results using PMMA as an e-beam resist to fabricate blazed optical structures in 1982 [38]. Applying grayscale e-beam lithography in PMMA, they were able to fabricate Fresnel zone plates with 50% efficiency. The

---

[1] Only the resists that are available in our laboratory are discussed here. There are other e-beam resists, for example X AR-N 7220, that are suitable for grayscale lithography, but are not included here.

development condition was 1:1 MIBK[2]/IPA[3] at 10℃. The work was followed up by Teruhiro Shiono, et al. in 2002[39]. Reflective gratings with 0.54-10$\mu$m period with 800nm maximum feature height were fabricated. Gratings with efficiency as high as 95%, fine control of blazed structure, and relatively flat surfaces under SEM were achieved.

### Choice of developer

The PMMA development condition we chose is 1:1 MIBK/IPA mixture at 16℃for 90 seconds. This mixture gives acceptable surface roughness while maintaining a relatively low clearing dose for the PMMA thickness we are using. This also avoids possible cross-linking of the PMMA at high dose [40].

## 5.2.2 Dose matrices in PMMA with SEBL

### PMMA sample preparation process

The SPPs were patterned using SEBL on both doped silicon and glass substrates. After spinning 800nm of PMMA on the substrate, a one hour oven bake at 180℃was applied. No conductive layer on PMMA was required for silicon substrates, whereas a thin conductive layer was coated on top of PMMA for glass substrates. Samples were patterned at 30 keV acceleration voltage using a commercial SEBL tool, the Raith-150$^{\text{TM}}$. The PMMA was developed in a 1:1 MIBK/IPA mixture for 90 seconds and rinsed with IPA.

### Two different conductive layers

We investigated two different conductive layers: 5nm aluminum and Aquasave$^{\text{TM}}$, a water soluble conducting polymer.

Although metal coating is a very commonly used as conductive layers on top of insulating samples for e-beam lithography, many problems occurred for grayscale

---

[2] methyl isobutyl ketone

[3] isopropanol

fabrication. First of all, evidences show that the aluminum residue on PMMA affects the development rate of PMMA. Over-etching of aluminum may ensure that the aluminum is completely removed, but the aluminum etchant (KOH) is also known to affect PMMA. Moreover, the partially developed PMMA is rough, opaque, and soft, compromising the efficiency and durability of the optic. This problem is illustrated in the optical micrographs in Fig. 5-6. The partially developed PMMA regions were readily scratched by the tip of the profilometer. Post-baking the partially developed PMMA helps increase its transparency, but the surface uniformity is still poor.

**(a)** **(b)** **(c)**

Figure 5-6: Optical micrographs of partially developed PMMA boxes after SEBL grayscale patterning (a) with 5nm aluminum conductive coating before post-baking and (b) after post-baking for 1hr at 180°Cin the oven, and (c) with Aquasave$^{\mathrm{TM}}$ as the conductive layer. The lines in the boxes are from scratching of the tip of the profilometer during depth measurements. This shows that partially developed PMMA is soft.

In contrast, with Aquasave$^{\mathrm{TM}}$ conductive coating, the partially developed PMMA exhibit less surface roughness and preserves optical transparency, as shown in Fig. 5-6 (c). The contrast curves for the 1:1 MIBK/IPA developer are shown in Figs. 5-7 (a) and 5-7 (b). Note that since the penetration depth of electrons at 30 keV is on the order of a micron, the first 2-3 $\mu$m of the substrate is still important. This explains the slight shift of the dose curve between samples on silicon wafers and glass wafers. However, the fact that the two curves are very close to each other is sufficient to prove that the Aquasave layer almost eliminates the charging effect of the PMMA-on-glass sample. The Auaqsave$^{\mathrm{TM}}$ layer also conducts as well as the 5nm aluminum layer, as shown in Fig. 5-8. Therefore, we decided to use Aquasave$^{\mathrm{TM}}$ with one hour oven

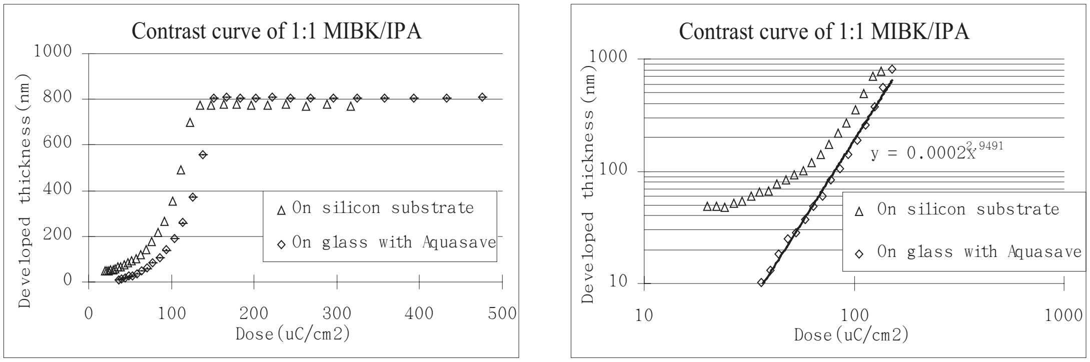

**(a)** **(b)**

Figure 5-7: The developed depth of PMMA verses dose curve for 1:1 MIBK/IPA developer on silicon and glass substrates in (a) linear and (b) log scales. The contrast curve of the Aquasave-coated PMMA is highly reproducible and gives sensitivity as high as the samples on silicon wafers.

bake at 90℃as the conductive layer for our finalized SPP fabrication process.

### 5.2.3 SPP in PMMA with SEBL

The maximum phase step required for an SPP is $2\pi$, which corresponds to a step height $\Delta l_{max}$ in PMMA of 816nm (index of refraction, $n_{PMMA} = 1.49$ at $\lambda$=400nm). A schematic of the SPP design, the SEBL grayscale-dose distribution, and the expected phase profile are shown again in Figure 5-9. The depth, $d$, of each wedge shown in Fig. 5-9 is given by $d = \Delta l_{max}\phi/(2\pi)$, where $\phi$ is the azimuthal angle. The dose for each wedge was calculated by interpolation from the contrast curve in Figs. 5-7 (a) and 5-7 (b). A Linnik interferogram and a scanning-electron micrograph of the fabricated SPP are shown in Fig. 5-10. These reveal problems with this fabrication technique. First, the grooves developed along the boundaries of the wedges arise from limitations of the patterning strategy. The electron beam dwells longer at the boundaries in order to allow the currents in the deflection coils of the SEBL to settle. This results in over-exposure at the boundaries. Second, the Gaussian tail of the point-spread function (PSF) of the scanning-electron beam produces sloped resist profiles at the wedge boundaries. In addition, because of the thick PMMA used, the

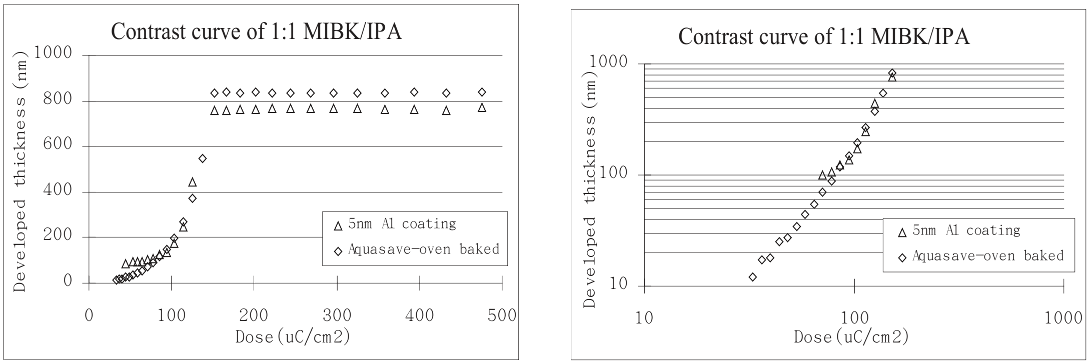

**(a)** **(b)**

Figure 5-8: The developed depth of PMMA verses dose curve for 1:1 MIBK/IPA developer with 5nm Al and Aquasave as conductive layer on glass substrates in (a) in normal scale (b) in double-log scale. The Auqsave layer conducts as well as the 5nm aluminum layer.

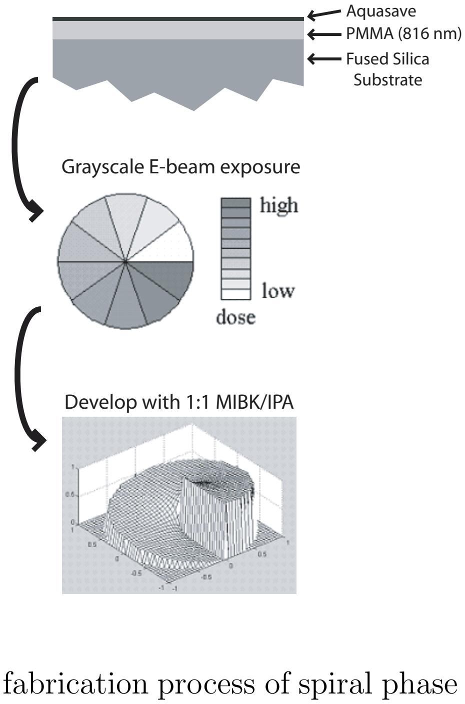

Figure 5-9: Schematic of fabrication process of spiral phase plates. PMMA is spun on a glass substrate to a thickness corresponding to a $2\pi$ phase shift. The electron beam dose is varied in wedges along the azimuthal direction as shown. The exposed PMMA is developed in a solution of MIBK and IPA in the ratio 1:1. Partial development of the PMMA results in a spiral height (phase) variation.

PSF at different depths may be slightly different, making proximity-effect correction difficult. The partially developed PMMA is soft, compromising the durability of the optic. These problems associated with grayscale SEBL prompted us to look for other diffractive elements.

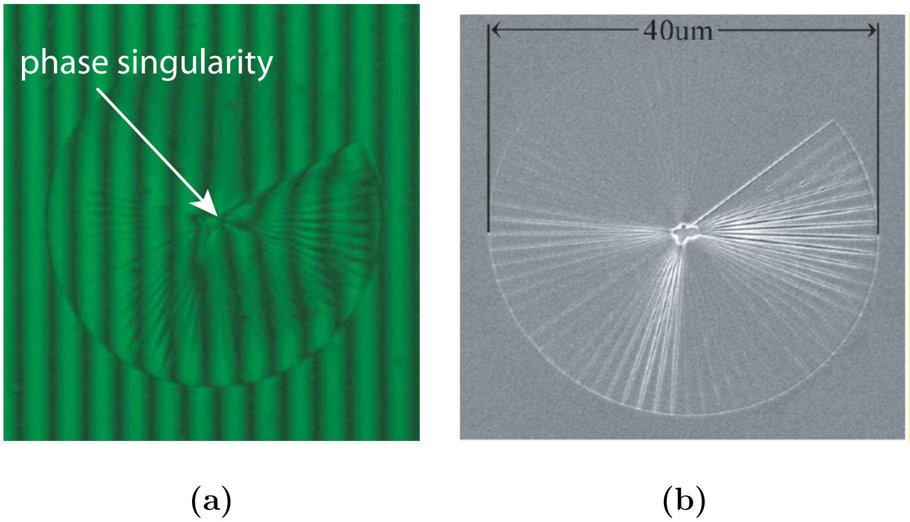

Figure 5-10: (a) A LINNIK interferogram of a fabricated SPP, revealing the height profile of the spiral in PMMA. The phase singularity at the center is clearly visible as a fork in the line fringes. (b) A scanning-electron micrograph of the fabricated SPP.

## 5.3 Binary Spiral Zone Plates

In this section, we report on the fabrication of binary phase SZPs in PMMA, descrbe the characterization of their optical performance via photoresist exposures, and compare the results to theory.

### 5.3.1 Design Formula and E-beam Patterning Strategy

A schematic of an SZP is shown again in Fig. 5-13 (a). The intensity at the node is minimized when light passing through adjacent zones is phase shifted by $\pi$ radians. Since we use PMMA as our phase shifter, the height difference between adjacent zones is achieved by controlling the thickness of the PMMA while spin-coating. PMMA was spun on a double-side-polished fused-silica substrate. The fabrication process consists of patterning with SEBL and development in 1:3 MIBK/IPA. A $\pi$-phase shift at $\lambda$ =532nm in PMMA ($n_{PMMA}$=1.49 at $\lambda$=532nm) requires zone height of 543nm (h= $0.5*\lambda/(n_{PMMA} - n_{Air})$).The boundaries of the spiral zone are determined by the following equations [36]:

$$\theta = 0.5\pi + r^2/\lambda R = 0.5\pi + 2r^2\frac{NA}{\lambda D}\sqrt{1+(\frac{D}{2R})^2} \tag{5.4}$$

$$\theta = 1.5\pi + r^2/\lambda R = 1.5\pi + 2r^2\frac{NA}{\lambda D}\sqrt{1+(\frac{D}{2R})^2} \tag{5.5}$$

where r and $\theta$ are the polar coordinates on the SZP plane, $\lambda$ is the wavelength of the incident light, $f$ is the focal length of the SZP, NA is the numerical aperture of the SZP, and D is the diameter of the SZP. Fig. 5-11 shows an example for Eq. 5.4 and Eq. 5.5.

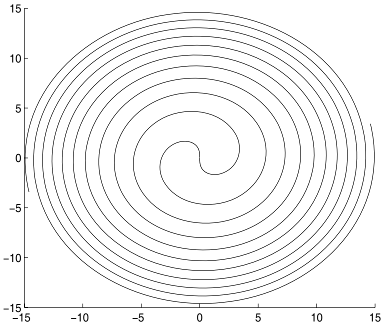

Figure 5-11: An example for the two boundaries described in Eq. 5.4 and Eq. 5.5. The two boundaries meets at the origin (0,0).

One of the two spiral zones is filled with single-pixel lines illustrated with dashed lines in Fig. 5-12. The normal vector at each point of the boundary is calculated by taking the minus inverse of the local slope, which can be calculated using the position difference from adjacent points. With a predefined step size (18nm in the final process) and proper definition of the sign of the normal vectors, we can compute the spiral lines inside the boundary by moving each point inward with the step size recursively until the spiral zone is locally filled. Due to the limitation of maximum 1000 points on each single-pixel line, each complete spiral line consists of a different number of single-pixel line segments, depending on the length of the spiral line. A complete spiral line is written from the outmost zone of one boundary, to the center of the spiral, then to the other boundary, and back to the outmost zone of the other boundary. Note that the number of single-pixel lines required to fill the zone at different parts of the spiral zones is different simply because the zone width is different. Therefore, the closer a spiral line gets to the center of the spiral zone, the shorter the spiral line becomes.

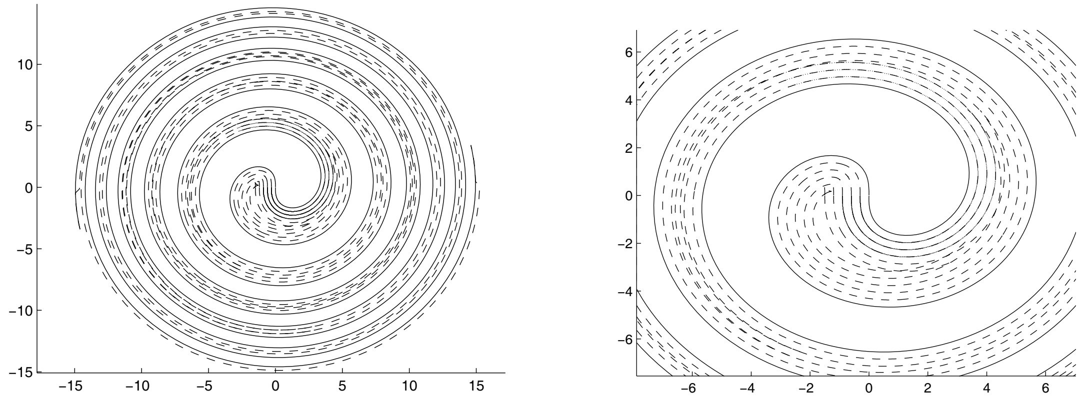

**(a)** **(b)**

Figure 5-12: (a) An illustration of how the spiral zone is filled in with single-pixel lines. (b) A zoomed in view at the center of the spiral.

### 5.3.2 Fabrication Process

The spiral zone was patterned using the Raith-150$^{\mathrm{TM}}$ at an acceleration voltage of 30 keV. The fabrication process, along with scanning-electron micrographs of a completed SZP, is shown in Fig. 5-13. A monolayer of HMDS was spun on a 3-inch double-side polished fused silica substrate before spinning PMMA to promote adhesion. A thin layer of aluminum is deposited on top of the PMMA by electron-beam evaporation to serve as a conductive layer to prevent pattern distortions due to charging. After patterning, the aluminum is removed by a one-minute etch in CD-26. The PMMA is developed using a 1:3 MIBK/IPA mixture for 90 seconds.

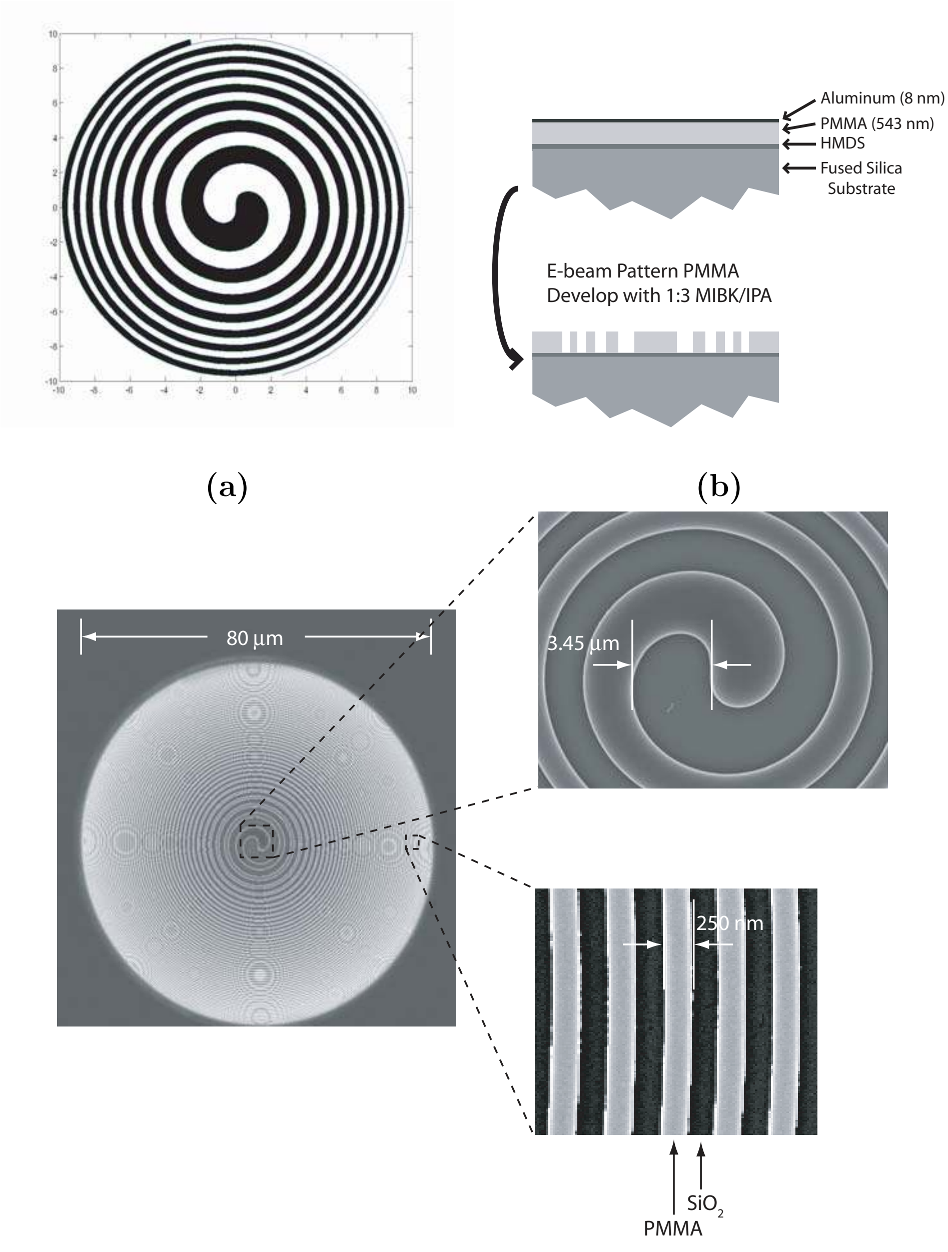

**(a)** **(b)**

**(c)**

Figure 5-13: (a) Schematic of the binary spiral zone plate. The black region is phase shifted by $\pi$ with respect to the white region. (b) Schematic of fabrication process. PMMA is spun on top of a glass substrate to a thickness corresponding to a $\pi$ phase shift. The exposed PMMA is developed in a solution of MIBK and IPA in the ratio 1:3. (c) Scanning-electron micrographs of a spiral zone plate with NA=0.7.

### 5.3.3 Performance Evaluation and Simulation Results

The point-spread-function (PSF) of the spiral zone plate (SZP) was characterized and compared to theory. The highly nonlinear behavior of positive photoresists such as PMMA enables one to assume a threshold model of resist development. This approximation allows one to reconstruct the PSF by exposing single spots over a range of doses, and measuring the radii of the corresponding spots [41]. In order to ensure proper gapping between the recording substrate and the SZPs, three zone plates designed for 632nm wavelength, but having the same focal lengths as the SZPs (40m), were fabricated around the SZPs. The gap was set to the focal length of the SZP by monitoring a confocal signal generated by these "satellite" zone plates, when illuminated by $\lambda = 632$nm. This procedure has been described elsewhere [42].

The photoresist was PFI-88, a positive-tone I-line resist from Sumitomo Chemicals. Although designed to be sensitive to I-line radiation, PFI-88 has a low sensitivity at 532nm. We exposed single spots at times ranging from 10 minutes to 25 minutes. A micrometer-controlled stage was manually operated to separate the spots by 10 micrometers. The inner and outer radii of the exposed spots were measured using a scanning-electron microscope. The data was scaled such that the inner radius at the lowest exposed dose matched the corresponding value of the normalized theoretical PSF. The simulation is done by Rajesh Menon,and the results are shown in 5-14. The measured PSF was best fit to the theoretical PSF at a defocus of 1.1$\mu$m. The theoretical PSF at focus is also shown for comparison. A scalar Fresnel-Kirchoff diffraction model was used to simulate the PSF. At present, the reason for the mismatch between the measured and the calculated PSFs is not known. It is possible that stage drift, laser power instability, focus errors and other process variations might be responsible. Photoresists with higher sensitivity at 532nm wavelength could reduce the effect of stage instability and background exposure.

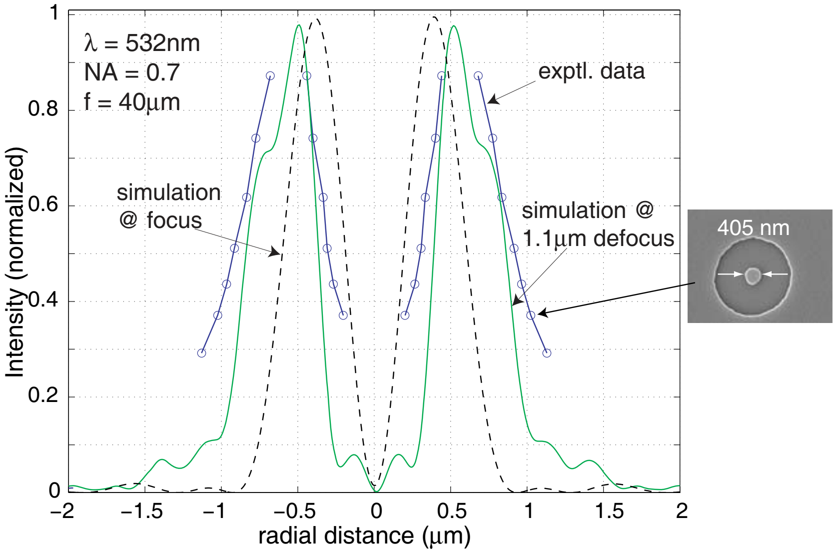

Figure 5-14: Characterization of the point-spread function (PSF) of the spiral zone plate designed to focus $\lambda = 532$nm at a numerical aperture (NA) of 0.7. The experimentally determined PSF is shown by connected circles (in blue). A scanning-electron micrograph of an exposed spot is shown in the inset. Note that both the inner and outer radii of the exposed spots were measured. The theoretical PSF at focus is shown as a dashed line (in black). It was empirically determined that the experimental data was best matched to the theoretical PSF at a defocus of $1.1\mu$m, which is shown as a solid green curve. The theoretical PSFs were calculated using the Fresnel-Kirchoff diffraction theory. Calculations are done by Rajesh Menon.

# Chapter 6

# Conclusion

The research described in this thesis has established the promising potential of absorbance-modulation optical lithography (AMOL) to initiate a new era in optical lithography in much the same way that the research of S. Hell and colleagues on STED initiated a new era in fluorescence microscopy. In that work the so-called diffraction barrier of optical microscopy was broken, more than 100 years after Ernst Abbe' established the fundamental limits of conventional optical microscopy. The key idea in AMOL as in STED is the use of an optical null in conjunction with appropriate reversible photochemistry. It is this author's opinion that further research on AMOL can not only lead to efficient nano-scale lithography, but also microscopy with resolution nearly comparable to scanning-electron microscopy (SEM) with optical means. Future study will focus on proper materials for the absorbance-modulation layer (AML,) the recording system, and the fabrication of dichromatic elements that generates the light beams required by AMOL to demonstrate the capability of AMOL predicted by theory.

# References

[1] H.I. Smith, R. Menon, A. Patel, D. Chao, M. Walsh, and G. Barbastathis. Zone-plate-array lithography: A low-cost complement or competitor to scanning-electron-beam lithography. *Microelectronic Engineering*, 83(4-9):956–961, 2006.

[2] S. Sun and G.J. Leggett. Matching the Resolution of Electron Beam Lithography by Scanning Near-Field Photolithography. *NANO LETTERS*, 4:1381–1384, 2004.

[3] T. Ito, T. Yamada, Y. Inao, T. Yamaguchi, N. Mizutani, and R. Kuroda. Fabrication of half-pitch 32 nm resist patterns using near-field lithography with a-Si mask. *Applied Physics Letters*, 89:033113, 2006.

[4] A.N. Boto, P. Kok, D.S. Abrams, S.L. Braunstein, C.P. Williams, and J.P. Dowling. Quantum Interferometric Optical Lithography: Exploiting Entanglement to Beat the Diffraction Limit. *Physical Review Letters*, 85(13):2733–2736, 2000.

[5] JB Pendry. Negative Refraction Makes a Perfect Lens. *Physical Review Letters*, 85(18):3966–3969, 2000.

[6] CG Willson. In Introduction to Microlithography, ; Thompson, LF; Willson, CG; Bowden, MJ, Eds, 1994.

[7] M. Feldman. Phase shift microscopes. *Journal of Vacuum Science & Technology B: Microelectronics and Nanometer Structures*, 16:3647, 1998.

[8] AP Chu, KK Berggren, KS Johnson, and MG Prentiss. A virtual slit for atom optics and nanolithography. *Quantum Semiclass. Opt*, 8:521, 1996.

[9] KS Johnson et al. Localization of Metastable Atom Beams with Optical Standing Waves: Nanolithography at the Heisenberg Limit. *Science*, 280(5369):1583–1586, 1998.

[10] KK Berggren, A. Bard, JL Wilbur, JD Gillaspy, AG Helg, JJ McClelland, SL Rolston, WD Phillips, M. Prentiss, and GM Whitesides. Microlithography by using neutral metastable atoms and self-assembled monolayers. *Science*, 269(5228):1255, 1995.

[11] S.W. Hell and J. Wichmann. Breaking the diffraction resolution limit by stimulated emission: stimulated-emission-depletion fluorescence microscopy. *Opt. Lett*, 19(11):780–782, 1994.

[12] S.W. Hell. Strategy for far-field optical imaging and writing without diffraction limit. *Physics Letters A*, 326(1-2):140–145, 2004.

[13] E. Engel, N. Huse, TA Klar, and SW Hell. Creating?/3 focal holes with a Mach–Zehnder interferometer. *Applied Physics B: Lasers and Optics*, 77(1):11–17, 2003.

[14] V. Westphal and S.W. Hell. Nanoscale Resolution in the Focal Plane of an Optical Microscope. *Physical Review Letters*, 94(14):143903, 2005.

[15] Rajesh Menon and Henry I. Smith. Absorbance-modulation optical lithography. *J. Opt. Soc. Am. A*, 23(9):2290, 2006.

[16] A.A. Patel. *The Development of a Prototype Zone-Plate-Array Lithography (ZPAL) System.* PhD thesis, Massachusetts Institute of Technology, Dept. of Electrical Engineering and Computer Science, 2004.

[17] D. Gil, R. Menon, and H.I. Smith. Fabrication of high-numerical-aperture phase zone plates with a single lithography exposure and no etching. *Journal of Vacuum Science & Technology B: Microelectronics and Nanometer Structures*, 21:2956, 2003.

[18] D. Chao, A. Patel, T. Barwicz, H.I. Smith, and R. Menon. Immersion zone-plate-array lithography. *Journal of Vacuum Science & Technology B: Microelectronics and Nanometer Structures*, 23:2657, 2005.

[19] BF Griffing and PR West. Contrast enhanced photolithography. *Electron Device Letters, IEEE*, 4(1):14–16, 1983.

[20] J.C. Crano and R.J. Guglielmetti. *Organic photochromic and thermochromic compounds Volume 2 Physicochemical studies, biological applications and thermochromism Topics in applied chemistry.* Kluwer Academic/Plenum Publishers, 1999.

[21] M.D. Levenson, T.J. Ebihara, G. Dai, Y. Morikawa, N. Hayashi, and S.M. Tan. Optical vortex masks for via levels. *Journal of Microlithography, Microfabrication, and Microsystems*, 3:293, 2004.

[22] M.S. Ho, A. Natansohn, C. Barrett, and P. Rochon. Azo polymers for reversible optical storage. 8. The effect of polarity of the azobenzene groups. *Canadian Journal of Chemistry*, 73(11):1773–1778, 1995.

[23] C. Barrett, A. Natansohn, and P. Rochon. Cis-Trans Thermal Isomerization Rates of Bound and Doped Azobenzenes in a Series of Polymers. *Chemistry of Materials*, 7(5):899–903, 1995.

[24] A. Bianco, C. Bertarelli, MC Gallazzi, G. Zerbi, E. Giro, and E. Molinari. Smart focal plane masks: rewritable photochromic films for astronomical multi-object spectroscopy. *Astronomische Nachrichten*, 326(5):370–374, 2005.

[25] Rajesh Menon, Hsin-Yu Tsai, and Samuel W. Thomas III. Far-Field Generation of Localized Light Fields using Absorbance Modulation. *Physical Review Letters*, 98:043905, 2007.

[26] Kurt Ronse. Assessing the challenges of EUV lithography. *Solid State Technology*, 50(2):64, 2007.

[27] S. Owa, A. Hazelton, and H. Magoon. Immersion lithography for 45nm manufacturing: fulfilling the manufacturing potential of immersion lithography requires tool designs that deal successfully with flare, lens heating, overlay, throughput and defectivity issues. *Microlithography World*, 16(1):4, 2007.

[28] Kevin M. Monahan. Addressing 32nm half-pitch challenges with double-patterning lithography. *Solid State Technology*, 49(12):28, 2006.

[29] A.M. Biswas, J. Li, J.A. Hiserote, and L.S. Melvin III. Extension of 193 nm dry lithography to 45-nm half-pitch node: double exposure and double processing technique. *Proceedings of SPIE*, 6349:63491P, 2006.

[30] V. Garcés-Chávez, K. Volke-Sepulveda, S. Chávez-Cerda, W. Sibbett, and K. Dholakia. Transfer of orbital angular momentum to an optically trapped low-index particle. *Physical Review A*, 66(6):63402, 2002.

[31] G. Donnert, J. Keller, R. Medda, M.A. Andrei, S.O. Rizzoli, R. Luhrmann, R. Jahn, C. Eggeling, and S.W. Hell. Macromolecular-scale resolution in biological fluorescence microscopy. *Proceedings of the National Academy of Sciences*, 103(31):11440, 2006.

[32] M.D. Levenson, G. Dai, and T. Ebihara. The vortex mask: making 80nm Contacts with a twist! *Proc. SPIE*, 4889:1293–1303, 2002.

[33] T. Watanabe, M. Fujii, Y. Watanabe, N. Toyama, and Y. Iketaki. Generation of a doughnut-shaped beam using a spiral phase plate. *Review of Scientific Instruments*, 75:5131, 2004.

[34] JAO Huguenin, B. Coutinho dos Santos, PAM dos Santos, and AZ Khoury. Topological defects in moire fringes with spiral zone plates. *Journal of the Optical Society of America A*, 20(10):1883–1889, 2003.

[35] S. Sinzinger and J. Jahns. *Microoptics.* Wiley-VCH, 2003.

[36] NR Heckenberg, R. McDuff, CP Smith, and AG White. Generation of optical phase singularities by computer-generated holograms. *Opt. Lett*, 17(3):221–223, 1992.

[37] V.V. Kotlyar, A.A. Almazov, S.N. Khonina, V.A. Soifer, H. Elfstrom, and J. Turunen. Generation of phase singularity through diffracting a plane or Gaussian beam by a spiral phase plate. *Journal of the Optical Society of America A*, 22(5):849–861, 2005.

[38] T. Fujita, H. Nishihara, and J. Koyama. Blazed gratings and Fresnel lenses fabricated by electron-beam lithography. *Opt. Lett*, 7:578–580, 1982.

[39] T. Shiono, T. Hamamoto, and K. Takahara. High-efficiency blazed diffractive optical elements for the violet wavelength fabricated by electron-beam lithography. *Appl. Opt*, 41(13):2390–2393, 2002.

[40] R. Murali, D.K. Brown, K.P. Martin, and J.D. Meindl. Process optimization and proximity effect correction for gray scale e-beam lithography. *Journal of Vacuum Science & Technology B: Microelectronics and Nanometer Structures*, 24:2936, 2006.

[41] R. Menon, D. Gil, and H.I. Smith. Experimental characterization of focusing by high-numerical-aperture zone plates. *Journal of the Optical Society of America A*, 23(3):567–571, 2006.

[42] D. Gil, R. Menon, DJD Carter, and H.I. Smith. Lithographic patterning and confocal imaging with zone plates. *Journal of Vacuum Science & Technology B: Microelectronics and Nanometer Structures*, 18:2881, 2000.